JℲM PAPERS

Flow and coherent structures generated by a circular array of rigid, emerged cylinders in a shallow channel

Kyoungsik Chang[1], Chenyu Jiang[2,3], George Constantinescu[3,†] and Yeong-Ki Jung[4]

[1] School of Mechanical Engineering, University of Ulsan, Ulsan, 44610, Korea

[2] Water Conservancy Development Research Center of Taihu Basin Authority of Ministry of Water Resources, Shanghai 200438, PR China

[3] IIHR-Hydroscience and Engineering and Department of Civil and Environmental Engineering, The University of Iowa, Iowa City, IA 52240, USA

[4] Mechanical R&D Laboratory, LIG Nex1, Seongnam, 13488, South Korea

The study investigates the flow structure, dynamics of the large-scale coherent structures, drag forces and sediment entrainment mechanisms generated by a circular array of diameter D containing rigid emerged circular cylinders of diameter d placed in a smooth-bed channel of depth h under strong shallow flow conditions ($D/h = 20$, $d/D = 0.0125$ and 0.025). Eddy resolving simulations are conducted with different values of the solid volume fraction $0.025 \leq SVF \leq 0.1$ and non-dimensional frontal area per unit volume ($2.56 \leq aD \leq 10.2$, where for the present configuration, $a = SVF(1/d)4/\pi$) and a fixed channel Reynolds number ($Re_h = 10\,000$). The flow conditions are such that a vortex street (VS)-type of shallow wake is expected to form for a solid cylinder of diameter D. Findings are compared with previous results obtained for cases with moderately shallow conditions $2.5 \leq D/h \leq 3.5$ and with the limiting case of flow past a solid cylinder with $D/h = 20$. For moderately shallow conditions, the core of the main horseshoe vortex (HV) forming around the array occupies a small fraction of the water column and its coherence is the largest in front of the array. By contrast, for very shallow conditions, multiple HVs form around the array and their cores occupy a large fraction of the water column. Moreover, the coherence of most of these HVs peaks close to the sides of the array. Only for relatively large aD values, the main HV extends over the whole upstream face of the array, similar to the limiting case of a solid cylinder. For sufficiently high aD, a secondary instability is present inside the near wake that leads to the formation of parallel horizontal vortices in the

† Email address for correspondence: sconstan@engineering.uiowa.edu

vicinity of the wake roller vortices. The changes in the wake structure with decreasing SVF and aD are qualitatively similar to those observed for cases with moderately shallow flow conditions, with the antisymmetric wake shedding mode being suppressed for $aD \leq 2.5$. However, the Strouhal number associated with the shedding of wake rollers, which is still close to 0.2 for a solid cylinder with $D/h = 20$, can be as high as 0.4 for $aD = 2.5$. The paper also discusses how the steady wake and total wake lengths and the strength of the bleeding flow vary with the SVF. Simulation results show that the capacity of the flow to entrain sediment inside and around the array peaks for $SVF = 0.05$ and $aD = 5.2$, with sediment entrainment monotonically increasing with the SVF outside the array and monotonically decreasing inside the array. Despite the differences in the flow structure next to and inside the array, the variation of the mean, time-averaged streamwise drag coefficient of the solid cylinders $\bar{C}_d$ with aD is close to that observed for arrays with moderately shallow flow conditions. The combined drag coefficient for the array decreases with increasing flow shallowness, with the decay being stronger for relatively large values of aD.

Key words: shallow water flows, river dynamics

1. Introduction

The flow past isolated arrays of solid vertical cylinders placed on a bottom surface has been made the object of numerous experimental (e.g. see White & Nepf 2007; Liu *et al.* 2008; Rominger, Lightbody & Nepf 2010; Zong & Nepf 2010, 2011, 2012; Rominger & Nepf 2011; Chen *et al.* 2012; Kim, Kimura & Shimizu 2015; Lei & Nepf 2021) and numerical investigations (e.g. see Huai, Xue & Qian 2015; Chang, Constantinescu & Tsai 2017, 2020; Koken & Constantinescu 2020, 2023; Liu *et al.* 2021). These studies were mainly motivated by the need to understand flow and transport processes past patches of aquatic canopies present in the main channel of rivers and/or over their floodplains. Aquatic canopies in fluvial systems alter the local flow dynamics and create coherent structures in their wake thus influencing transport and mixing processes (Nepf 2012).

Aquatic canopies in the form of patches of emerged and submerged vegetation occupying various parts of river channels and floodplains (Carr, Duthie & Taylor 1997; Sukhodolov & Sukhodolova 2010) play several important ecological roles (Jones, Lawton & Schachak 1994; Costanza *et al.* 1997; Corenblit *et al.* 2007; Gurnell 2014). They create regions with enriched nutrients, enhanced light penetration and oxygen levels, and increased plant productivity (Wilcock *et al.* 1999; Horppila & Nurminen 2003; Schultz *et al.* 2003; Schoelynck *et al.* 2012; Camporeale *et al.* 2013). Vegetation canopies reduce the transport capacity of rivers due to increased plant-induced drag (Tal & Paola 2007; Plew, Cooper & Callaghan 2008). Canopies also create flow acceleration zones near the patch boundaries which causes bed erosion (Follett & Nepf 2012; Liu & Nepf 2016) and nutrient limitation (negative feedback for patch growth). Finally, canopies generate large-scale coherent structures and increased turbulence in the river reach (Righetti & Armanini 2002; Liu *et al.* 2008; Zong & Nepf 2012; Pan *et al.* 2014; Chang *et al.* 2017; Koken & Constantinescu 2020, 2023). Nutrient transport within canopies and plant nutrient uptake depend on the vertical momentum, secondary flow and turbulence intensity within the canopy. Turbulence, especially near the canopy front and its sides, inhibits deposition and resuspension, leading to bed scouring (Souliotis & Prinos 2010; Pan *et al.* 2014; Sukhodolov & Sukhodolova 2014; Kim *et al.* 2015; Yang, Chung & Nepf 2016). Inside canopies, sediment deposition and nutrient accumulation are enhanced, while sediment erosion is reduced (Gurnell *et al.* 2005; Bouma *et al.* 2007;

van Wesenbeck *et al.* 2008; Schoelynck *et al.* 2012; Liu & Nepf 2016; Liu *et al.* 2017). This benefits ecosystem productivity by promoting canopy growth (Sukhodolov & Sukhodolova 2014; Liu *et al.* 2017).

In the case of patches of emergent vegetation, the width of the patch is generally much larger than the flow depth, especially for vegetation growing over the floodplain at low flooding conditions. In the case of braided rivers, the ratio between the (maximum) width of these patches, D, and the mean flow depth, h, is often larger than 10. For such conditions, flow shallowness effects associated with bed friction and large values of D/h are expected to strongly affect flow, transport and sediment entrainment mechanisms around, inside and downstream of the patch. For very shallow conditions, the dynamics of the large-scale eddies generated in the wake of porous obstacles (e.g. plant stems) may be strongly affected by their interaction with the channel bed (Prinz, Brevis & Socolofsky 2012). Moreover, the vertical development of the large-scale structures forming in the wake and around the patch (e.g. horseshoe vortices) is constrained by both the free surface and the channel bed. These phenomena are expected to be qualitatively similar to those observed for shallow wakes developing behind solid obstacles (e.g. solid circular cylinders with $D/h \gg 1$) which made the object of several experimental, numerical and stability theory studies (e.g. see Chen & Jirka 1995; Grubisic, Smith & Schar 1995; Balachandar, Ramachandran & Tachie 2000; Socolofsky, Carmer & Jirka 2004; Negretti *et al.* 2005; Rockwell 2008; Carmer, Rummel & Jirka 2009; Zeng & Constantinescu 2017). One of the most striking differences between a deep wake and a shallow wake is that the rate of growth of the latter decays with increasing distance from the obstacle. This is accompanied by a gradual loss of coherence of the wake billows, or wake roller vortices, once their average diameter becomes much larger than the flow depth and they start behaving as quasi-two-dimensional coherent structures. As these structures are advected over the (no slip) bed surface, their energy decays mainly due to dissipation at the bed surface. At sufficiently large distances from the obstacle, the wake region contains only small-scale turbulence and its width becomes close to constant (Balachandar, Chu & Zhang 1997). The dynamics is similar to what is also observed in shallow mixing layers (Cheng & Constantinescu 2020).

Several experimental investigations and stability theory studies have shown that three main types of flow patterns are observed inside the wake with increasing flow shallowness (Chen & Jirka 1995; Socolofsky *et al.* 2004; Socolofsky & Jirka 2004; Carmer *et al.* 2009). The change from one type to the other is mainly a function of the value of a non-dimensional number called the stability number $S_s = c_f D/h$, where c_f is the bed friction coefficient. This number characterizes the stabilizing influence of the channel bed on the large-scale eddies developing inside the near wake (Ingram & Chu 1987; Chen & Jirka 1995). For $S_s < 0.2$, quasi-two-dimensional wake rollers are shed in the wake. This vortex street (VS) regime resembles the von Kármán vortex street observed for deep wakes but wake stabilization occurs with increasing distance from the obstacle. The unsteady bubble (UB) regime is observed for $0.2 < S_s < 0.5$. In this regime, a large unsteady bubble forms at the back of the obstacle and a turbulent wake of sinusoidal shape is present behind the bubble, but no wake rollers form. In the steady bubble (SB) regime observed for $S_s > 0.5$, the recirculation bubble is quasi steady and the wake contains no growing instabilities.

In addition to the wake region, flow shallowness also affects the physics of the horseshoe vortices (HVs) forming around the base of solid obstacles. While in the case of a deep channel flow the average diameter of the main HVs is much smaller than the flow depth, the two length scales become comparable for $D/h \gg 1$. Moreover, the structure of the flow inside the HV region also changes with increasing D/h. Zeng & Constantinescu (2017)

have shown that the dynamics of the HVs forming around a solid cylinder with $D/h \geq 10$ resembles the one associated with the laminar breakaway regime (Kirkil & Constantinescu 2012). For such very shallow cases, the primary HV is not subject to aperiodic bimodal oscillations as generally observed for deep and moderately shallow flow conditions (e.g. see Kirkil & Constantinescu 2015). The other consequence of the cores of the HVs extending until close to the free surface is that the interactions between their legs and the separated shear layers forming on the two sides of the obstacle are not limited to the near-bed region. For very shallow conditions, the legs of these HVs can strongly affect the interactions between the two separated shear layers over the whole flow depth. Zeng & Constantinescu (2017) have shown that one consequence of these interactions is the generation of a secondary instability in the form of co-rotating, parallel, horizontal vortices forming in the vicinity of the wake rollers for cases where the VS regime is observed in the wake. Akilli & Rockwell (2002) and Carmer *et al.* (2009) also found that three-dimensional (3-D) effects in the wake become more important with increasing flow shallowness. Their study found that horizontal (braid) vortices form in between successively shed roller vortices and that the flow moves upwards inside the core of the roller vortices.

Despite their relevance for fluvial hydraulics, the physics of shallow wakes past porous, isolated obstacles in a channel was not yet investigated using modern experimental and numerical techniques that allow a quantitative characterization of the dynamics of the coherent structures forming around and inside the wake of the obstacle, and of the flow interactions with the individual elements of the porous obstacle. A main reason is that most experimental investigations of flow past isolated patches containing emerged plant stems or rigid cylinders were caried out in flumes that are not wide enough to accommodate patches with $D/h \gg 5$ while maintaining a fairly low blockage ratio (e.g. width to diameter ratio larger than 5), a sufficiently high channel Reynolds number and being able to perform accurate measurements over the flow depth. Eddy resolving simulations that resolve the flow past the individual elements (e.g. plant stems, cylinders) of the porous obstacle, though computationally very expensive, are not subject to the aforementioned limitations (Chang & Constantinescu 2015; Monti, Omidyeganeh & Pinelli 2019; Monti *et al.* 2020). Such an approach allows obtaining detailed quantitative information on the drag forces acting on individual cylinders, the flow and turbulence inside the array, and the bed shear stresses. Such simulations also allow characterizing the coherent structures, their dynamics and their interactions with the channel bed, something that is very complicated to achieve via experimental investigations (Chang *et al.* 2020).

The present study uses detached eddy simulation (DES) to investigate flow past a circular array of diameter D containing N rigid, emerged circular cylinders of diameter d placed in a straight and wide open channel (figure 1) for very shallow flow conditions ($D/h = 20$). The incoming flow is fully developed and turbulent. The channel Reynolds number is $Re_h = 10\,000$. The circular shape of the array eliminates the angle of attack as a major variable that needs to be considered for arrays of other shapes. Moreover, close-to-circular shapes are very common for vegetation patches forming away from the river banks especially during their early growth stages (Sand-Jensen & Pedersen 2008). Though vegetated canopies are often characterized by volume heterogeneity (Hamed *et al.* 2017) and flexibility (Hong *et al.* 2022, Houseago *et al.* 2022), the study of a constant porosity or, equivalently, of a constant solid volume fraction (SVF) array serves as a base case with respect to which the effects of such complexities can be better evaluated for shallow flow conditions. In addition to d/D, the other relevant non-dimensional length scale is aD, where a is the frontal area per unit volume (e.g. $a = Nd/(\pi D^2/4)$
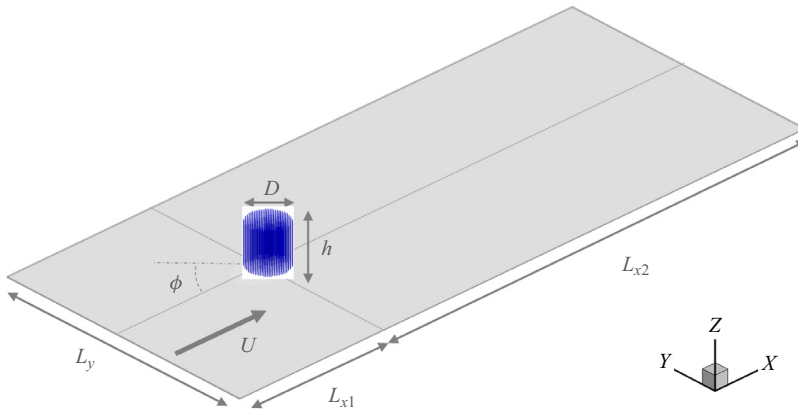
Figure 1. Sketch of the computational domain containing a circular array of solid cylinders. The emerged array of diameter D is placed in an open channel with incoming bulk velocity U and flow depth h. The polar angle ϕ is measured with respect to the symmetry plane ($y/D = 0$) upstream of the centre of the array.

for circular cylinders). In the case of an array containing circular cylinders of constant diameter, $a = \text{SVF}(1/d)4/\pi$. So, varying a, or aD, is equivalent to varying the SVF if d and D are kept constant. Given that the total force acting on the array scales with a rather than the SVF, comparison of results for circular arrays with close values of aD is generally more relevant for cases where the diameter of the solid cylinders forming the array is different (Zong & Nepf 2012). For the geometrical and flow conditions considered, the value of the stability number is $S_s = 0.13$. So, the VS regime is expected to be observed in the wake of the array, at least for sufficiently high SVF.

   The main goal of the present paper is to investigate the flow structure around and inside arrays of emerged circular cylinders with $D/h = 20$ for which the flow conditions can be classified as very shallow. A second goal is to investigate differences with respect to wakes past arrays of cylinders generated for deep and moderately shallow conditions. In particular, the present study tries to answer the following questions.

  (i) What is the structure of the horseshoe vortex system for circular arrays with a large D/h?
 (ii) Does the suppression of the antisymmetric shedding mode for shallow wakes in the VS regime occur at approximately the same values of SVF and aD as those observed for wakes past circular arrays with $D/h < 5$ (e.g. for wakes in the deep or moderately shallow regime)?
(iii) Is the dependence of some of the main non-dimensional variables characterizing the wake region (e.g. lengths of steady wake and total wake regions non-dimensionalized using the array diameter, D, Strouhal number associated with formation of wake rollers) and of the total streamwise drag force (e.g. mean drag coefficient acting on the cylinders forming the array, combined total drag parameter) with aD similar to that observed for arrays with $D/h < 5$?
 (iv) What are the main sediment erosion mechanisms around and inside circular arrays with a large D/h? How does the erosive capacity of the flow vary with increasing SVF for such arrays?

   The paper is organized as follows. Section 2 briefly describes the flow solver and the DES module, the test cases, the boundary conditions and the relevant validation studies

conducted using the same DES flow solver. Section 3 analyses how the SVF and *d/D* affect the formation of the horseshoe vortices, their position, size, circulation and dynamics. Section 4 investigates how *aD* affects the wake structure behind the array, 3-D effects, as well as some of the variables used to characterize the wake flow behind porous obstacles (e.g. the lengths of the steady wake and total wake regions). Section 5 investigates the bed friction velocity distributions in the mean and instantaneous flow fields and the role of the large-scale coherent structures in explaining sediment erosion inside and around the array. Section 6 discusses how the total non-dimensional streamwise drag force, the mean drag coefficient for the cylinders forming the array and the combined drag parameter for the array vary with *aD*. Results are also compared with those obtained for arrays with moderately shallow flow conditions. Section 7 summarizes the main findings and presents some conclusions.

2. Numerical approach

2.1. *Numerical method and governing equations*

The eddy-resolving simulations are performed using DES. DES combines Reynolds-averaged Navier–Stokes (RANS) modelling near solid boundaries with large eddy simulation (LES) away from these boundaries (Spalart 2009). The turbulence length scale in DES is redefined away from solid boundaries such that it becomes proportional to the cell size, similar to LES (Chang, Constantinescu & Park 2007; Rodi, Constantinescu & Stoesser 2013). The one-equation Spalart–Allmaras (SA) model (Spalart & Allmaras 1992) is used as the base turbulence model in the present DES simulations.

The incompressible Navier–Stokes equations are solved together with the transport equation for the modified eddy viscosity, $\tilde{\nu}$. The continuity and momentum equations are

$$\frac{\partial u_i}{\partial x_i} = 0, \tag{2.1}$$

$$\frac{\partial u_i}{\partial t} + \frac{\partial (u_i u_k)}{\partial x_k} = -\frac{1}{\rho}\frac{\partial p}{\partial x_i} + \frac{\partial}{\partial x_k}\left[(\nu + \nu_t)\left(\frac{\partial u_i}{\partial x_k} + \frac{\partial u_k}{\partial x_i}\right)\right], \tag{2.2}$$

where ρ is the constant density, u_i is the resolved velocity component in the *i*th direction, *p* is the resolved hydrostatic pressure, *t* is the time, x_i is the coordinate in the *i* direction, ν_t is the subgrid-scale viscosity provided by the SA-based DES model and ν is the kinematic viscosity. The transport equation for $\tilde{\nu}$ is

$$\frac{\partial \tilde{\nu}}{\partial t} + u_j\frac{\partial \tilde{\nu}}{\partial x_j} = C_{b1}\tilde{S}\tilde{\nu} + \frac{1}{\sigma}[\boldsymbol{\nabla}\cdot((\nu+\tilde{\nu})\boldsymbol{\nabla}\tilde{\nu}) + C_{b2}(\boldsymbol{\nabla}\tilde{\nu})^2] - C_{w1}f_w\left[\frac{\tilde{\nu}}{l}\right]^2, \tag{2.3}$$

where the turbulence length scale *l* is defined as the minimum between the distance to the closest wall surface, l_{min}, and $C_{DES}\Delta$. The cell size Δ is defined as the minimum length of the cell along the three directions. The sub-grid scale viscosity is calculated as

$$\nu_t = f_{v1}\tilde{\nu}, \tag{2.4}$$

where f_{v1} is a damping function. The other variables and model parameters are

$$\tilde{S} = \bar{S} + (\tilde{\nu}/\kappa^2 l^2)f_{v2}, \tag{2.5a}$$

$$f_{v2} = 1 - (\tilde{\nu}/\nu)/(1 + \chi f_{v1}), \tag{2.5b}$$

$$f_{v1} = \frac{\chi^3}{\chi^3 + C_{\nu1}^3}, \tag{2.5c}$$

$$\chi = \frac{\tilde{\nu}}{\nu}, \tag{2.5d}$$

$$f_w = g'\left[\frac{1 + C_{w3}^6}{g'^6 + C_{w31}^6}\right]^{1/6}, \tag{2.5e}$$

$$g' = r + C_{w2}(r^6 - r) \tag{2.5f}$$

$$r = \frac{\tilde{\nu}}{\tilde{S}\kappa^2 l^2}, \tag{2.5g}$$

where $\bar{S}$ is the magnitude of the resolved vorticity vector and κ is the von Kármán constant. The model constants are $C_{DES} = 0.65$, $C_{b1} = 0.135$, $C_{b2} = 0.622$, $\sigma = 0.67$, $\kappa = 0.41$, $C_{\nu1} = 7.1$, $C_{w2} = 0.3$, $C_{w3} = 2.0$ and $C_{w1} = C_{b1}/\kappa^2 + (1 + C_{b2})/\sigma$.

The governing equations were transformed to generalized curvilinear coordinates (Zeng, Constantinescu & Weber 2008). The use of a surface conforming structured mesh allows specifying no-slip boundary conditions on the surface of the cylinders. A blanking procedure was used to account for the presence of cylinders inside the computational domain. The 3-D incompressible Navier–Stokes equations were integrated using a fully implicit fractional-step method. The convective terms in the momentum equations and the transport equation for $\tilde{\nu}$ were discretized using a blend between the fifth-order accurate upwind biased scheme and the second-order central scheme. All other terms in the momentum equations and in the Poisson equation solved for the pressure were approximated using second-order central differences. The discrete momentum (predictor step) and turbulence model equations were integrated in pseudo-time using the alternate-direction-implicit approximate factorization scheme. Time integration was performed using a dual time-stepping algorithm by adding a pseudo time-derivative term in the momentum and transport equation for $\tilde{\nu}$. This term reduces to zero as convergence is achieved at each physical time step. The time discretization was second-order accurate. The mesh size in the wall-normal direction was sufficiently small to avoid the use of wall functions. Detailed descriptions of the non-hydrostatic, viscous flow solver and DES model are given in Chang *et al.* (2007, 2017).

The DES code was validated for several classes of open channel flows that are directly relevant for the applications discussed in the present study. Cheng & Constantinescu (2020) and Constantinescu (2014) discuss detailed validation for spatially developing shallow mixing layers in open channels with an aspects ratio of $O(100)$ and a channel length to flow depth ratio of several hundreds. The code successfully predicted the velocity profiles and the passage frequency of the Kelvin–Helmholtz rollers at different locations as well as transition towards the equilibrium regime where the growth of the mixing layer width is negligible. Kirkil & Constantinescu (2012, 2015) discuss validation for flow past a solid cylinder placed in an open channel with $D/h \cong 1$ and $1000 < Re_D < 10^6$. Chang *et al.* (2017) discuss validation for flow past a circular array of emerged solid cylinders with $D/h = 2.5$ and 3.3. The profiles of the mean velocity and lateral velocity fluctuations

along the array's centreline and the shedding frequency of the wake billows were found to be in good agreement with the experimental data of Zong & Nepf (2012) and Chen *et al.* (2012).

2.2. *Model set-up and boundary conditions*

The horizontal set-up of the present numerical simulations (figure 1) is similar to that used in the related studies of Chang *et al.* (2017, 2020) conducted for circular arrays with $D/h < 3.5$. In the present simulations, the bed is located at $z = -h$. The top boundary is situated at $z = 0$. The origin of the system of coordinates is located at the centre of the circular array. The streamwise direction is x, while the spanwise direction is y. The channel width is $L_y = 140h$, while the distances between the centre of the array and the inlet and outlet sections are $L_{x1} = 75h$ and $L_{x2} = 250h$, respectively (figure 1). As for the simulations conducted by Chang *et al.* (2017), the solid cylinders are placed using a close-to-regular staggered pattern in the x–y planes with a random displacement of $0.5d$–$2.0d$ with respect to a regular staggered pattern. This arrangement is similar to that used in laboratory experiments of flows past vegetated canopies with rigid cylinders (e.g. see Chen *et al.* 2012).

The horizontal mesh contained close to three million cells and 36 points were used to resolve the flow in the vertical direction. The mesh was refined inside the array and some distance downstream of it. In the vertical direction, the mesh was refined close to the bed surface. Away from the array, the non-dimensional sizes of the cells in the horizontal and vertical directions were close to those used by Cheng & Constantinescu (2020) and Zeng & Constantinescu (2017) to perform simulations of shallow mixing layers and flow past a solid cylinder with $20 \leq D/h \leq 50$, respectively. These simulations were also conducted in wide and long open channels with $L_y/h = O(100)$ and $(L_{x1} + L_{x2})/h > 200$, and with $Re_h \approx 10\,000$. The grid spacing at the bed in the wall-normal direction was $0.0025h$, corresponding to approximately one wall unit.

The turbulent flow at the channel inlet was fully developed, with a bulk channel velocity, U. A convective boundary condition was used at the outflow of the domain (Rodi *et al.* 2013). As in the previous simulations of flow past arrays of cylinders performed using the present DES solver, the top boundary was modelled as a shear-free horizontal rigid lid, which is justified given the relatively low channel Froude number. The solid surfaces were assumed to be smooth. The modified eddy viscosity was set equal to zero at the solid surfaces. Symmetry boundary conditions were used at the two lateral boundaries. The estimated value of the bed friction coefficient in the incoming flow was $c_f = 0.0064$. The time step was $dt = 0.0125h/U$. Its value was sufficiently low to resolve the range of energetic frequencies associated with the dynamically important coherent structures in the flow (e.g. horseshoe vortices, vortices shed in the wake of the solid cylinders, vortex tubes in the array's separated shear layers). In all critical regions of the flow containing large-scale eddies, the Courant number was much less than one. Mean flow and turbulence statistics were collected over a time interval of approximately $1000h/U$.

The number of cylinders in the array, N, and the diameter of the solid cylinders, d, were the two main array parameters varied in the simulations. For a circular array containing circular cylinders, $SVF = Nd^2/D^2$ and $aD = SVF*(D/d)*4/\pi$. Thus, when comparing simulations with the same value of D/d, studying the effects of varying aD and SVF is equivalent. The two (non-dimensional) length scales controlling the total drag force acting on the array are $1/(aD)$ and d/D. The main geometrical and flow variables for the five simulations are given in table 1. Three of the simulations were conducted with constant d

	SVF$=0.025$	SVF$=0.05$	SVF$=0.1$	SVF$=0.1(2d)$	SVF$=1.0$
N	160	320	640	160	1
d/D	0.0125	0.0125	0.0125	0.025	—
D/h	20	20	20	20	20
Re_h	10 000	10 000	10 000	10 000	10 000
Re_D	200 000	200 000	200 000	200 000	200 000
Re_d	2500	2500	2500	5000	—
aD	2.56	5.1	10.2	5.12	—
Ad	0.032	0.0638	0.1275	0.128	—
C_d	0.520	0.334	0.177	0.325	1.53
Γ_D	1.365	1.791	2.005	1.847	—
St	—	0.4	0.25	0.36	0.22
U_1/U_0	0.35	0.23	0.10	0.20	0.0
U_1/U_2	0.24	0.14	0.07	0.14	0.0
L_{sw}/h	—	—	40	—	—
L_{sw}/D	—	—	2.0	—	—
L'_{sw}/h	80	40	30	43	—
L'_{sw}/D	4.0	2.0	1.5	2.1	—
L'_w/h	170	140	75	125	15
L'_w/D	8.5	7.0	3.8	6.25	0.7

Table 1. Main geometrical and flow variables of the test cases (N is the number of cylinders in the array; d is diameter of the solid cylinders; D is the diameter of the circular array; h is the flow depth, U is the channel bulk velocity, $Re_h = Uh/\nu$, $Re_D = UD/\nu$, $Re_d = Ud/\nu$, ν is the molecular viscosity, aD is the non-dimensional frontal area per unit volume for the array; U_1 is the centreline streamwise velocity at the upstream end of the steady wake region; U_2 is the maximum streamwise velocity of the flow on the sides of the array; L_{sw} and L'_{sw} are the steady wake lengths defined based on mean velocity and spanwise normal stresses, respectively; L'_w is the total wake length; St_D is the Strouhal number defined with U and D corresponding to the most energetic frequency in the wake of the array; C_D is the mean solid cylinder streamwise drag coefficient; $\Gamma_D = C_D aD/(1 - \text{SVF})$ is the combined drag parameter for the array.

($=0.0125D$) and varying number of cylinders ($N = 120$, 320 and 641). The corresponding values of the SVF were 0.1, 0.05 and 0.025, respectively. A fourth simulation was conducted with larger cylinders ($d = 0.025D$) and $N = 160$ such that SVF$= 0.1$. The range of SVFs was comparable to that ($0.024 \leq \text{SVF} \leq 0.23$) in the simulations of Chang *et al.* (2017) conducted with $D/h = 2.5$ and 3.33. Also included are results from a fifth simulation for the limiting case of flow past a solid cylinder (SVF$= 1.0$).

3. Horseshoe vortex system

The Q criterion is used in figure 2 to visualize the HV system in the mean flow associated with the array. The variable Q is defined as $Q = 0.5(\|\Omega\|^2 - \|S\|^2)(h^2/U^2)$, where $\|\Omega\|$ is the magnitude of the rotation rate tensor and $\|S\|$ is the magnitude of the rate of strain tensor calculated with the resolved velocities. Though horseshoe vortices form in all four simulations conducted with an array of cylinders, there are several important differences between the SVF$= 0.1$ case that has the largest value of aD and the other cases for which $aD \leq 5.12$. It is only in the SVF$= 0.1$ case (figure 2b) that the primary HV forming in the immediate vicinity of the array remains strongly coherent until the symmetry plane corresponding to a polar angle $\phi = 0°$. The polar angle is defined with respect to the symmetry plane $y/D = 0$ upstream of the centre of the array (figure 1). Its core and legs extend from the bed up to approximately $0.2h$ from the top boundary. For all the other cases shown in figure 2(c–e), no HVs are present in the mean flow
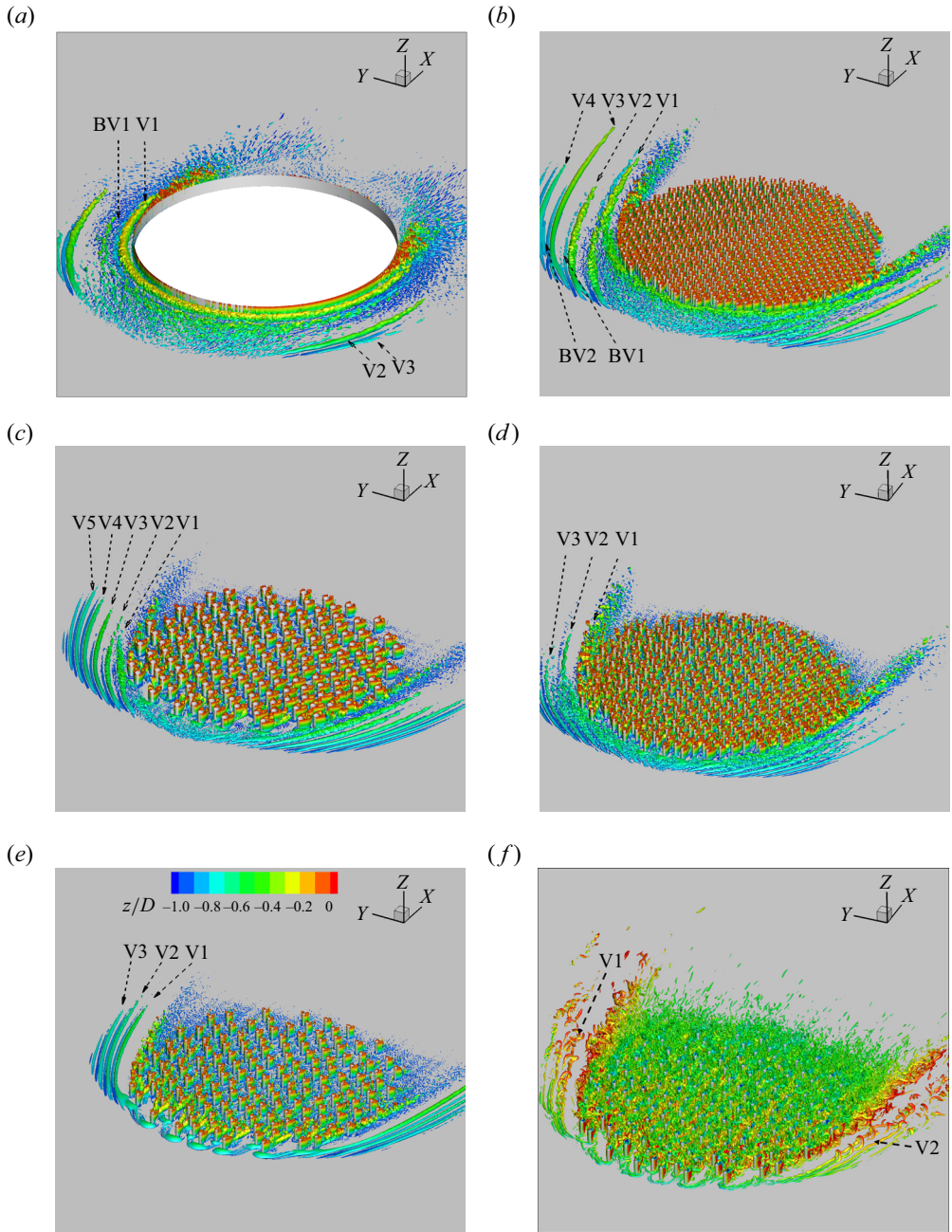
Figure 2. Visualization of the horseshoe vortex system using a Q isosurface ($Q = 0.1$). (*a*) SVF = 1.0 mean flow; (*b*) SVF = 0.1 mean flow; (*c*) SVF = 0.1(2*d*) mean flow; (*d*) SVF = 0.05 mean flow; (*e*) SVF = 0.025 mean flow; (*f*) SVF = 0.025, instantaneous flow. BV indicates a bottom-attached vortex. The colour contours represent the distance from the top boundary, z/D. Note the large-scale hairpins generated along the legs of the largest HV, V1 in panel (*f*).
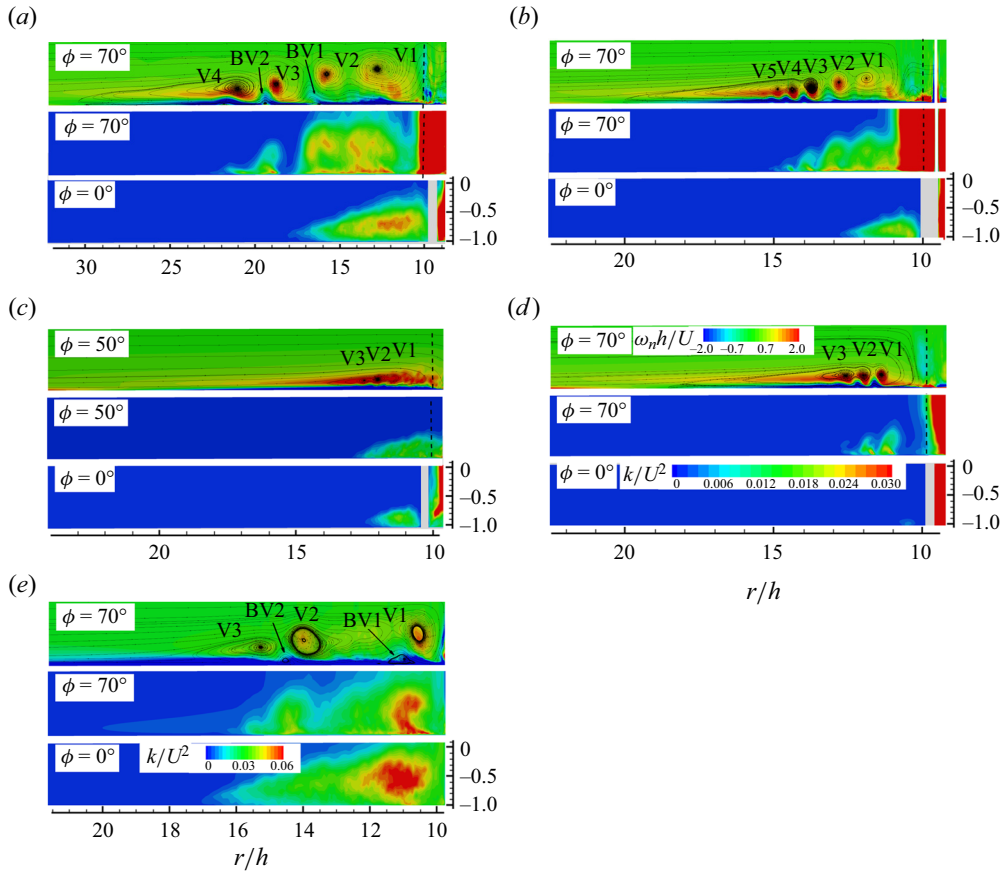
Figure 3. Visualization of flow structure inside the horseshoe vortex system in selected polar planes. (*a*) SVF = 0.1; (*b*) SVF = 0.1(2*d*); (*c*) SVF = 0.05; (*d*) SVF = 0.025; (*e*) SVF = 1.0. Top panels show the mean out of plane vorticity, $\omega_n h/U$, 2-D streamlines for $\phi = 70°$. Middle panels show the TKE, k/U^2, for $\phi = 70°$. Bottom panels show the TKE for $\phi = 0°$. The vertical dashed line indicates the boundary of the array. The interior of solid cylinders is represented in grey. The horizontal to vertical aspect ratio in all frames is 1:2.5. The radial distance measured from the origin of the array is r.

in between the symmetry plane and $|\phi| = 30°$–$40°$ except for the small HVs generated around the base of the cylinders directly exposed to the incoming flow. These vortices are clearly captured in figure 2(*e*,*f*) for the SVF = 0.025 case. Despite the absence of strongly coherent HVs in front of the array, the region situated close to the symmetry plane and the front face of the array is still characterized by high turbulent kinetic energy (TKE) levels (e.g. $k/U^2 > 0.01$) for $aD > 5$. This amplification of the TKE is mainly due to the smaller vortices that are shed from the region where the boundary layer separates (see TKE distributions in figure 3*b*,*c*). The size of this region and the peak TKE values inside it decay monotonically with decreasing aD (figures 3*a*–*d*). The turbulence amplification in the $\phi = 0°$ plane becomes negligible in the SVF = 0.025 case (figure 3*d*) where the HVs forming around the base of the cylinders directly exposed to the incoming flow are only subject to small oscillations around their mean flow position.

Results in figure 3 show that the overall level of TKE amplification inside the HV system region scales with aD rather than the SVF. This is not surprising as the pressure on the cylinders directly exposed to the incoming flow and the magnitude of the adverse
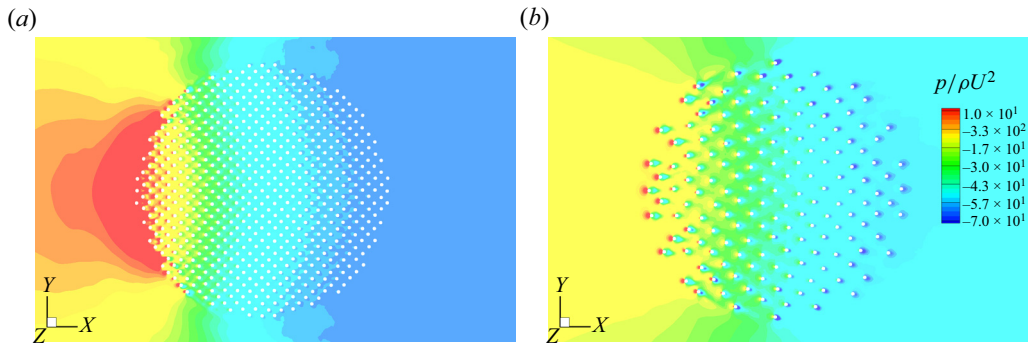
995 A9-11

(*a*)   (*b*)

Figure 4. Mean pressure, $p/\rho U^2$, at the top boundary ($z/h = 0$). (*a*) SVF = 0.1; (*b*) SVF = 0.025.

pressure gradients generated away from the frontal face of the array also scale with aD. For example, the mean non-dimensional pressure distributions on the top boundary (figure 4) show that the regions of high adverse pressure gradients are small and localized next to the upstream faces of the cylinders exposed to the incoming flow in the SVF = 0.025 case. In contrast, in the SVF = 0.1 case, the region of highest pressure magnitude extends from $\phi = -30°$ to $\phi = 30°$, with strong adverse pressure gradients generated upstream of it. So, for high aD, the region of increased pressure is associated with the array as a whole (e.g. with the porous obstacle) rather than with the individual cylinders forming the array. The coherence of the HV system mainly scales with the magnitude of the adverse pressure gradients generated away from the obstacle (Kirkil & Constantinescu 2015).

For the SVF = 1.0 and 0.1 cases, where the main HV remain strongly coherent for $0° < |\phi| < 90°$, the TKE levels are smaller in the SVF = 0.1 case compared with the SVF = 1.0 case (e.g. compare TKE distributions in figure 3*a,e*). This is a direct result of the decay of the adverse pressure gradients generated away from the upstream face of the array with decreasing SVF and aD. One interesting result is that the circulation of main horseshoe vortices V1 to V4 in the SVF = 0.1 case in the region where the coherence of these vortices is high ($30° < |\phi| < 90°$) is comparable to that of the corresponding vortices V1 and V2 in the SVF = 1.0 case. For both cases, the interaction of the main HVs with the bed generates the formation of bottom-attached vortices (see BV vortices in figure 3*a,e*).

The TKE distributions in the $\phi = 70°$ plane are representative for the region where the coherence of the HVs is the largest in the shallow flow simulations conducted with an array of cylinders. The number of vortices part of the HV system is not the highest for the case where coherence of these vortices, as measured by the size of their cores and their circulation, is the largest (see vorticity distributions in figure 3) and does not vary monotonically with aD or SVF. For $D/h = 20$, the number of HVs is equal to five in the SVF = 0.01(2*d*) case. This number decreases to four in the SVF = 0.1 case and to three in the SVF = 0.05 and 0.025 cases (figure 2). As discussed later, the main reason for the TKE amplification in this region is their advection towards the HV situated the closest to the array.

In the region of highest coherence of the HVs, the cores of the largest vortices extend approximately 0.6*h* in the vertical direction in the SVF = 0.1 case. This vertical length reduces to approximately 0.25*h*–0.3*h* in the SVF = 0.05 and SVF = 0.025 cases (see vorticity distributions in figure 3). By comparison, the core of the main turbulent HV forming around solid cylinders with $D/h \approx 1$ was approximately 0.25*h* (Kirkil & Constantinescu 2015). Large differences are also observed for the width of the HV

995 A9-12

system region. In the $\phi = 70°$ plane, HVs are present up to 7.5h (0.375D) away from the face of the array in the SVF = 0.1 case. This distance reduces to 3h (0.15D) in the SVF = 0.025 case. The value predicted for the SVF = 0.1 case is not very different from that (9h or 0.45D) predicted in the SVF = 1.0 case. By comparison, for moderately shallow conditions, Chang *et al.* (2017) found that the HV system region extended 0.25D away from the frontal face of the obstacle for a solid cylinder with $D/h = 2.5$ and approximately 0.2D for an array with SVF = 0.23, $aD = 9.6$ and $D/h = 2.5$. No HVs associated with the array were present in the other cases with $aD < 4.0$ investigated by Chang *et al.* (2017).

The presence of multiple vortices of comparable coherence inside the HV system and the fact that their coherence peaks for relatively high polar angle magnitudes are important differences with the HV system forming around arrays with $D/h < 4$ but with similar SVF and aD values (Chang *et al.* 2017). The structure of the HV system is also different from that observed in the case of flow around a solid circular cylinder with $D/h < 1$ where the HV system contains only one primary vortex that remain strongly coherent around the whole upstream face of the array. These differences are all induced by flow shallowness.

In the $D/h = 20$ cases, the dynamics of the cores of the main HVs resembles that of a laminar HV system in one of the breakaway sub-regimes containing two or more vortices (Kirkil & Constantinescu 2012). New HVs are shed from the region where the boundary layer separates while the cores of the other vortices advance towards the array. The core of V2 eventually merges with the core of the vortex situated the closest to the array (V1). As opposed to the case of solid cylinders with $D/h > 10$ (Zeng & Constantinescu 2017, there is no well-defined period associated with such a cycle in the present simulations conducted with $aD < 10$. This dynamic is also different from that observed for the turbulent HV system forming around solid bluff bodies for moderately shallow and deep flow ($D/h \ll 1$) conditions where the primary HV is subject to aperiodic bimodal oscillations and its interactions with small HVs shed from the region where the incoming boundary layer separates are fairly minor (Kirkil & Constantinescu 2015). One similarity with the dynamics of turbulent HVs forming around solid obstacles with $D/h < 1$ is that large-scale hairpins develop along the legs of the most coherent HVs in the instantaneous flow fields. For example, these hairpins can be observed in figure 2(*f*) for the SVF = 0.025 case, where their heads can raise up to approximately 0.4h above the bed surface. Only in the SVF = 0.1 case, the legs of the vortex situated the closest to the array, V1, strongly interact with the eddies shed in the separated shear layers over most of the flow depth. In all the other $D/h = 20$ cases, the HVs are situated relatively far from the array and/or their legs loose rapidly their coherence. This explains the weak interactions between the HVs and the separated shear layers in these cases.

4. Array and near wake regions

4.1. *Wake instabilities and coherent structures*

The distributions of the instantaneous vertical vorticity in horizontal planes show that a VS-type wake is present in the simulations conducted with SVF ≥ 0.05 and that the distance from the back of the array where roller vortices form increases with decreasing SVF and aD (e.g. see figure 5a,b). By contrast, wake billows do not form in the SVF = 0.025 case (figure 5c) where a turbulent wake undergoing undulatory motions forms behind a region of low velocities at the back of the array. This is somewhat similar to a UB-type wake behind a solid obstacle except that there is no recirculation bubble at the back of the array. So, the transition between the VS mode, where wake rollers form, and a wake mode, where the separated shear layers cannot interact, occurs
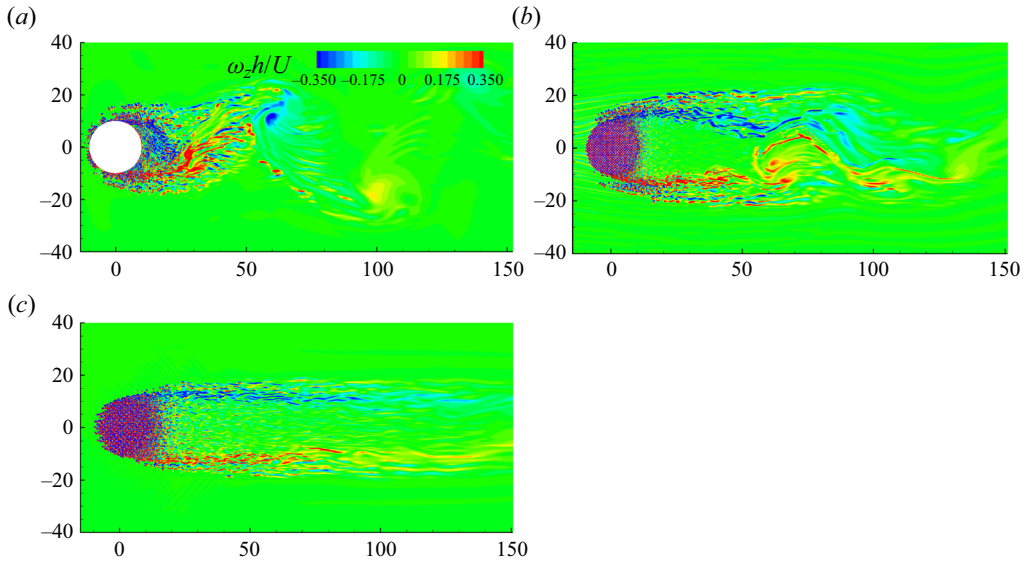
Figure 5. Non-dimensional vertical vorticity, $\omega_z h/U$, in the instantaneous flow close to the top boundary ($z/h = -0.1$). (a) SVF $= 1.0$; (b) SVF $= 0.1$; (c) SVF $= 0.025$.

at SVF values slightly smaller than 0.05. This value is very close to the threshold value observed by Chang *et al.* (2017) for moderately shallow conditions (the antisymmetric wake shedding mode was absent in their simulation conducted with SVF $= 0.034$) and also to the experimental results of Zong & Nepf (2011) and Chen *et al.* (2012). Based on this result, one can conclude that changes in the wake structure are not significantly affected by flow shallowness.

However, this is not the case for the dominant shedding frequency of the roller vortices, *f*. For moderately shallow conditions and sufficiently large SVF, for the antisymmetric wake shedding mode to be dominant, Chang *et al.* (2017) predicted values of the Strouhal number $St = fD/U$ between 0.22 (SVF $= 1$) and 0.2 (SVF $= 0.092$), consistent with values measured in experiments conducted for porous cylinders with similar values of D/h. In the present simulations, $St = 0.22$ for SVF $= 1.0$, which is very close to the range of values ($St = 0.21$–0.23) measured experimentally by Chen & Jirka (1995) for very shallow flow conditions with a VS-type wake forming behind the solid cylinder. The $St = 0.22$ value is slightly smaller than the values ($St = 0.25$–0.27) predicted for solid cylinders with $D/h \approx 1$ and $16\,000 < Re_D < 500\,000$ by Kirkil & Constantinescu (2015). Rather than being constant or slightly decreasing with decreasing aD and SVF, the Strouhal number in the simulations conducted with $D/h = 20$ increases monotonically with decreasing aD such that $St \approx 0.25$ for $aD \approx 10$ (SVF $= 0.1$ case) and $St \approx 0.36$–0.4 for $aD \approx 5$. So, flow shallowness has a major effect on the non-dimensional period associated with the interactions of the separated shear layers forming on the two sides of the array that result in the generation of wake rollers.

In the SVF $= 1.0$ (figure 5a) and SVF $= 0.1$ (figure 5b) cases, the legs of the main horseshoe vortices can get very close to the separated shear layers and interact with them (see figures 2a,b and 5a,b). For solid cylinders with $10 \leq D/h \leq 25$, Zeng & Constantinescu (2017) observed the formation of parallel corotating horizontal vortices close to the roller vortices. This 3-D near-wake instability is driven by the strong interaction of the horseshoe vortices with the separated shear layers. The instability is also present in the SVF $= 1$
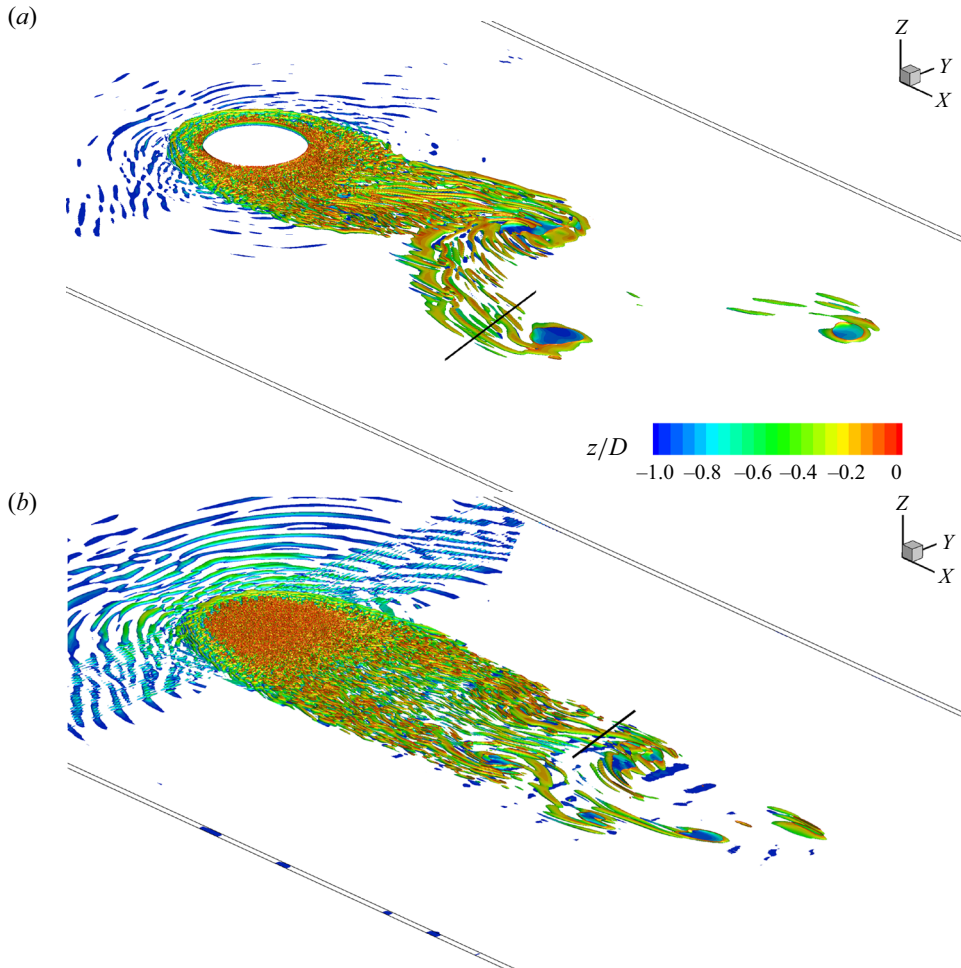
995 A9-14

(*a*)

z/D

−1.0 −0.8 −0.6 −0.4 −0.2 0

(*b*)

Figure 6. Visualization of coherent structures in the instantaneous flow using a Q isosurface ($Q = 0.002$). (*a*) SVF = 1.0; (*b*) SVF = 0.1. The black lines in panels (*a*) and (*b*) show the position of the x/h = constant planes shown in figure 7.

simulation (figure 6*a*) where these vortices are situated slightly behind and on the outer side, with respect to the symmetry plane, of the roller vortices. The length of these vortices can attain $10h$ or $0.5D$ and their spacing in the spanwise direction is of the order of $1h$ to $1.5h$. The streamwise velocity inside the cores of these vortices is smaller than that in the surrounding wake flow (figure 7*a*). Given that the cores of these vortices extend over approximately 80 % of the flow depth, they can play an important role in vertical mixing inside the near wake. Moreover, these vortices can have a strong effect on the transport of fine sediments and nutrients by advecting near-bed fluid towards the top boundary (e.g. free surface for a patch of vegetation in an open channel). Despite the common belief that shallow wakes are quasi-two-dimensional, strong 3-D instabilities can be generated because of flow shallowness. The present study also shows that this instability is also present in the case of arrays of cylinders provided that the non-dimensional frontal area per unit volume is sufficiently large such that strong interactions take place between the legs of the most coherent horseshoe vortices and the separated shear layers. Such streamwise
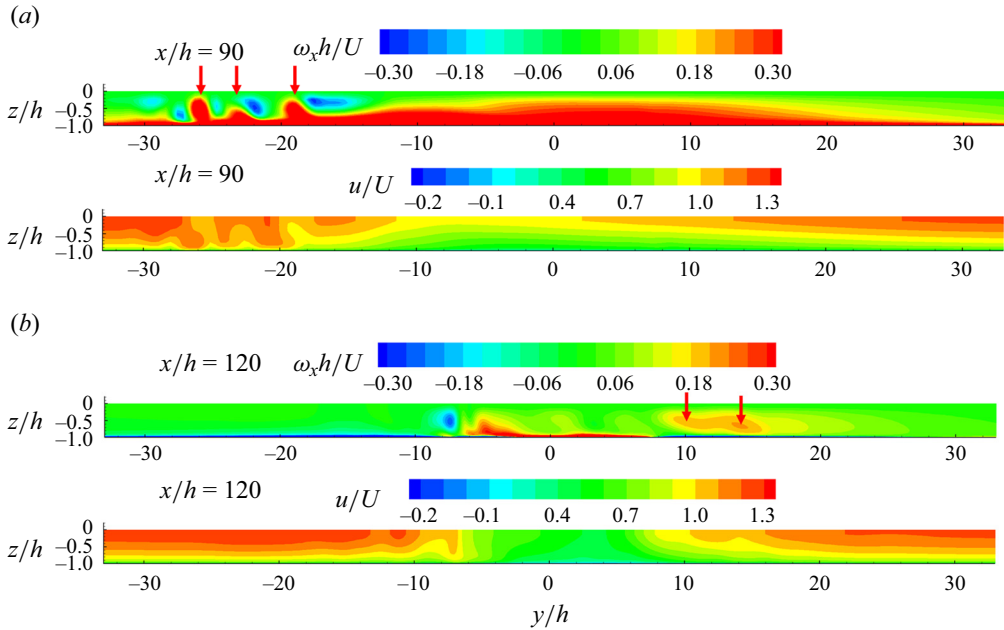
Figure 7. Streamwise vorticity, $\omega_x h/U$, (top panel) and streamwise velocity, u/U, (bottom panel) in an instantaneous flow field. (*a*) SVF $= 1.0$, $x/h = 90$; (*b*) SVF $= 0.1$, $x/h = 120$. The red arrows point towards patches of high streamwise vorticity associated with some of the streamwise-oriented vortices visualized in figure 6.

vortices form in the vicinity of the roller vortices only in the SVF $= 0.1$ simulation for which $aD = 10.2$ (figures 6*b* and 7*b*) but not in the other simulations with $aD \leq 5.2$. So, the threshold value of aD is between 5 and 10. As expected, the average circulation of the streamwise vortices in the SVF $= 0.1$ case is smaller compared with that of the corresponding vortices forming in the SVF $= 1.0$ simulation but the cores of these vortices still occupy a large fraction of the channel depth.

4.2. *Flow inside the array*

Despite the 2-D geometry, the flow inside the array is not quasi-two-dimensional. In the case of patches of vegetation, the secondary flow and vertical velocity fluctuations inside the array have important implications for trapping heavy metals and suspended sediments as well as for the transport of nutrients (Zong & Nepf 2011). The main 3-D effects are due to the downflow forming parallel to the upstream face of the array and, for sufficiently high SVFs, the rotational motion of the core of the horseshoe vortex situated in the immediate vicinity of the array. In the SVF $= 0.1$ case (figure 8*a*), which is the only case where a strongly coherent horseshoe vortex forms along the whole frontal face of the array, 3-D mean-flow effects are fairly limited and associated with the fluid moving with the downflow that penetrates slightly inside the array. As aD decreases, so do the coherence and diameter of the horseshoe vortices. As for the case of circular arrays with moderately shallow flow conditions (Chang *et al.* 2017), the flow entering the array has a strong velocity component oriented towards the bed. Given the incompressibility constraint, this downflow is compensated by strong upwelling taking place in the wake of the cylinders situated close to the frontal face of the array (e.g. see figure 8*b* for SVF $= 0.025$ where

995 A9-16

(*a*)

(*b*)

w/U

2.0×10^{-1}
1.2×10^{-1}
4.0×10^{-2}
-4.0×10^{-2}
-1.2×10^{-1}
-2.0×10^{-1}
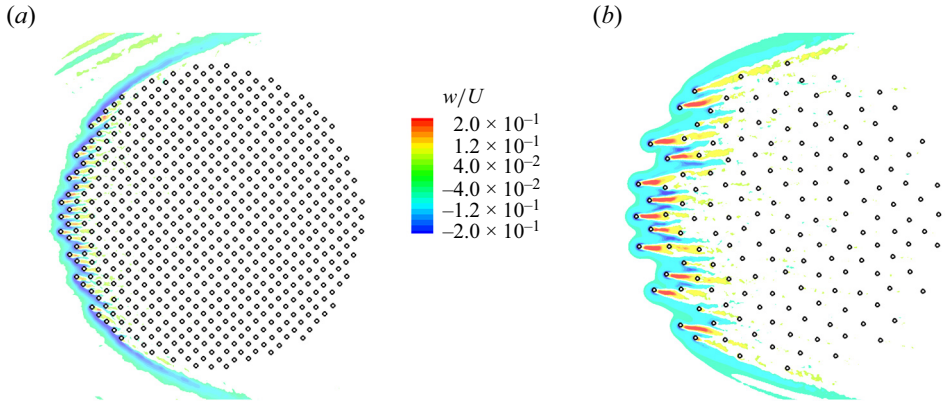
Figure 8. Non-dimensional mean vertical velocity, w/U, at mid depth ($z/h = -0.5$). Regions with $|w/U| < 0.04$ are blanked. (*a*) SVF $= 0.1$; (*b*) SVF $= 0.025$.
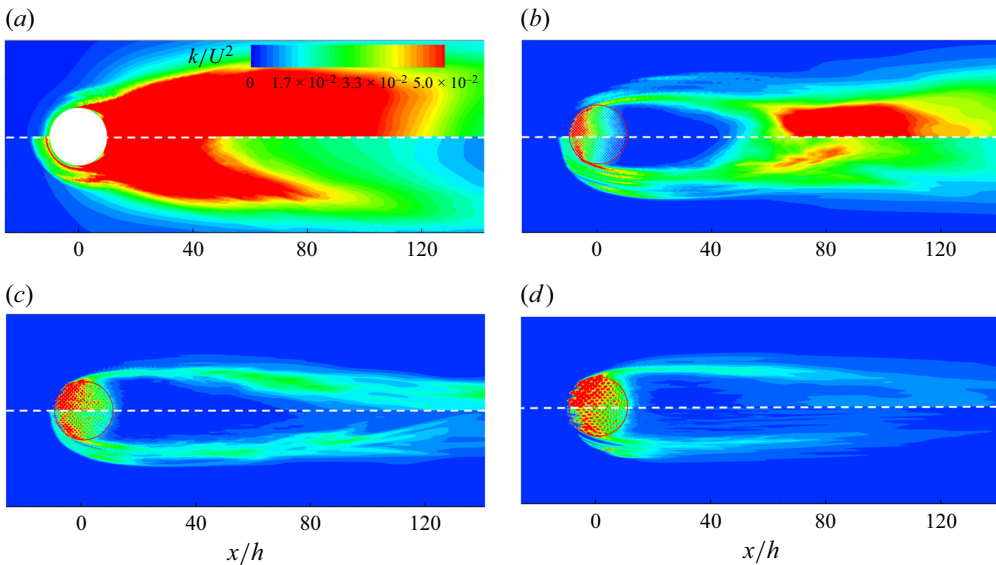
(*a*)

(*b*)

k/U^2

$0 \quad 1.7 \times 10^{-2} \quad 3.3 \times 10^{-2} \quad 5.0 \times 10^{-2}$

(*c*)

(*d*)

x/h

x/h

Figure 9. Non-dimensional TKE, k/U^2, close to the top boundary ($x/h = -0.1$, top half) and the channel bed ($z/h = -0.9$, bottom half). (*a*) SVF $= 1.0$; (*b*) SVF $= 0.1$; (*c*) SVF $= 0.05$; (*d*) SVF $= 0.025$. The red circle shows the boundary of the array region.

the peak vertical velocity magnitudes are of the order of $0.25U$). For similar values of aD, the upwelling and downwelling motions inside the array weaken with increasing flow shallowness (e.g. with increasing D/h).

The level of amplification of the TKE inside the array is directly related to the formation and shedding of vortices in the wake of the cylinders and the velocity magnitude in the flow approaching the cylinders. Close to the top boundary, the largest TKE is always observed near the front of the array (figure 9). However, for sufficiently low aD values, the largest TKE values close to the bed surface occur some distance behind the front face (e.g. see figure 9*d*). This effect is probably related to the downflow penetrating the array.

Similar to arrays of cylinders with $D/h = O(1)$ and to arrays of long cylinders (Chang & Constantinescu 2015; Chang *et al.* 2017), the horizontal flow inside the array is not oriented
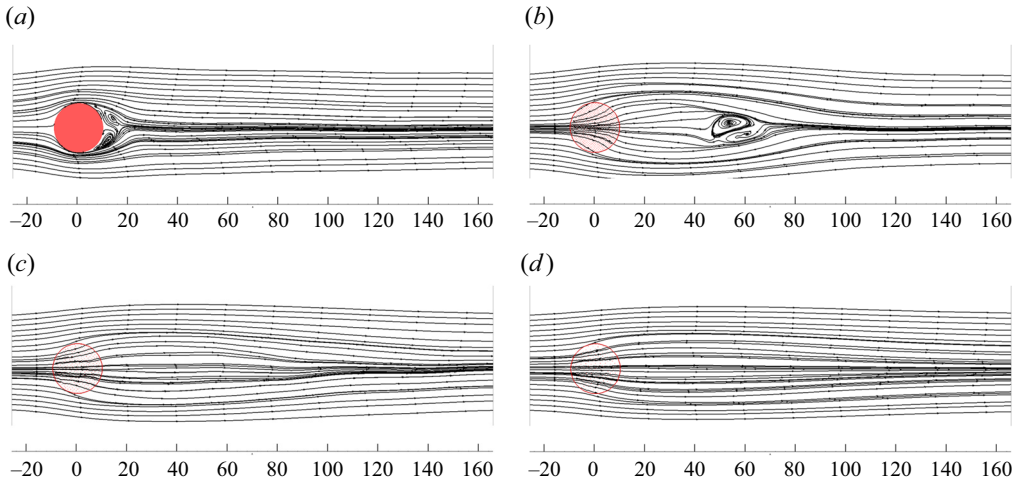
(*a*)

(*b*)

(*c*)

(*d*)

Figure 10. 2-D mean flow streamline patterns close to the top boundary ($z/h = -0.1$). (*a*) SVF = 1.0; (*b*) SVF = 0.1; (*c*) SVF = 0.05; (*d*) SVF = 0.025. The red circle shows the boundary of the array region.

along the streamwise direction. Rather, the flow entering the array diverges away from the symmetry plane, as shown by the mean streamline patterns in figure 10. This effect weakens with decreasing aD. The flow inside the array decelerates due to the drag induced by the cylinders. Table 1 reports the values of the bleeding flow velocity at the back of the array near the symmetry plane, U_1. The relative deceleration of the flow over the length of the array can be approximated as $(U - U_1)/U$. This value decreases with increasing aD from approximately 0.9 for $aD \approx 10$ to approximately 0.65 for $aD \approx 2.5$. Comparison with the simulations reported by Chang *et al.* (2017) shows that, for comparable values of aD, increasing the flow shallowness results in a slight reduction (e.g. by approximately 10 % as D/h increases from approximately 3 to 20) of the flow deceleration inside the array. This is mainly due to a slight decrease of the mean drag force acting on the cylinders with increasing flow shallowness, as will be discussed in § 6.

4.3. *Mean flow and turbulent kinetic energy inside the wake*

As for flow past emerged arrays with moderately shallow flow conditions, the near wake contains a recirculation bubble in the mean flow for cases where strong rollers are shed in the wake. The position and size of this bubble are mainly a function of aD. No bubble forms for cases when the antisymmetric vortex shedding mode is very weak or absent (e.g. see figure 10*c*,*d*). This is confirmed by comparison of the two SVF = 0.1 simulations. A fairly large bubble forms in the SVF = 0.1 case ($aD = 10.2$). No bubble forms in the SVF = 0.1(2*d*) case ($aD = 5.1$) and in the SVF = 0.05 case ($aD = 5.1$). Based also on the data of Chang *et al.* (2017), one can estimate the threshold value of aD to be close to 6 for a recirculating bubble to form in the wake of circular emerged arrays.

Comparison of the present simulation results with those of Chang *et al.* (2017) shows that the vertical non-uniformity of the bubble increases significantly with D/h. For $D/h = 20$ and SVF = 1.0, the length of the recirculation bubble increases from $0.5D$ near the top boundary to $0.7D$ near the bed. By contrast, the length of the same eddy was $0.7D$ at all flow depths for $D/h = 2.5$ (Chang *et al.* 2017). The differences increase when cases with $aD \approx 10$ are compared. For $D/h = 20$ and SVF = 0.1, the detached bubble starts at $x = 2.25D$ near the bed and at $x = 2.5D$, near the top boundary. The bubble

995 A9-18

length is close to $1.2D$ near the top boundary and $1.5D$ near the bed. Meanwhile, for $D/h = 2.5$ and $aD = 9.6$, the bubble length was $1.1D$ at all flow depths. So, increasing the flow shallowness decreases the two-dimensionality of the near-wake mean flow. The non-uniformity over the vertical direction of the flow and TKE decreases with decreasing aD especially once the roller vortices become very weak (SVF $= 0.05$ case) or do not form (SVF $= 0.025$ case). This can be seen by comparing the TKE distributions near the top boundary and near the bed in figure 9.

The steady wake is defined as the region where the mean streamwise velocity behind the array decreases (Zong & Nepf 2012). Its length is measured along the symmetry plane starting at the back of the array ($x/D = 0.5$). The end of the steady wake region approximatively corresponds to the length of the separated shear layers for the array. As the flow starts recovering inside the wake, the mean streamwise velocity in the symmetry plane starts increasing toward the free stream value. Zong & Nepf (2012) defined the length of the total wake region as the streamwise distance between the back of the array and the streamwise location where the rate of increase of the streamwise centreline velocity becomes very small (e.g. smaller than a threshold value). The longitudinal profiles of the streamwise velocity along the centreline ($y/D = 0$) in figure 11(*a*) show that a relative minimum associated with the end of the steady wake region is only observed in the SVF $= 0.1$ simulation. Following Chang & Constantinescu (2015), we use the longitudinal profiles of the spanwise normal stress $\overline{v'v'}$ along the centreline to identify the end of the steady wake and total wake regions. The end of the steady wake is defined as the location where $\overline{v'v'}$ starts increasing monotonically. The end of the total wake corresponds to the location where $\overline{v'v'}$ reaches its maximum (figure 11*b*). The lengths of the steady and total wake regions are measured from the back of the array and are denoted L'_{sw} and L'_w, respectively. This definition of L'_w has the advantage that it avoids defining an arbitrary threshold value for the streamwise velocity gradient along the centreline to identify the end of the total wake region. The streamwise variations of the centreline velocity and $\overline{v'v'}$ are close to identical in the SVF $= 0.1(2d)$ and SVF $= 0.05$ simulations for which $aD \approx 5.1$, which shows that aD rather than the SVF is the main parameter. Both variables are monotonically increasing with aD. Compared with arrays with $2.5 \leq D/h \leq 3.3$, the wake recovery is slower in the simulations conducted with $D/h = 20$. Moreover, the change from a streamwise velocity profile containing a relative minimum to one displaying a fairly monotonic increase over the whole wake occurs between $aD = 5$ and $aD = 10$ for $D/h = 20$ compared with $aD \approx 2$ for $2.5 \leq D/h \leq 3.3$.

The variations of L'_{sw}/D and L'_w/D with the ratio between the bleeding velocity at the back of the array, U_1, and the maximum streamwise velocity in the regions of flow acceleration on the two sides of the array, U_2, show a similar trend for the present simulations ($D/h = 20$) and for the simulations conducted by Chang *et al.* (2017) for arrays with $2.5 \leq D/h \leq 3.3$ (figure 12). However, for comparable aD values, L'_w/D is at least 30 % larger in the simulations conducted with $D/h = 20$.

5. Bed friction velocity and volumetric flux of entrained sediment

For flows past arrays of surface-mounted cylinders, large-scale turbulent eddies are a main contributor to erosion inside and around the array. Sediment can be entrained in regions where the mean bed friction velocity, $\bar{u}_\tau$, is less than the threshold value for sediment entrainment provided that the turbulence is strong near the bed (Yang *et al.* 2016). To characterize in an average way the capacity of the flow to entrain sediment at a certain location, one needs to consider not only the value of $\bar{u}_\tau$ but also the deviations of the
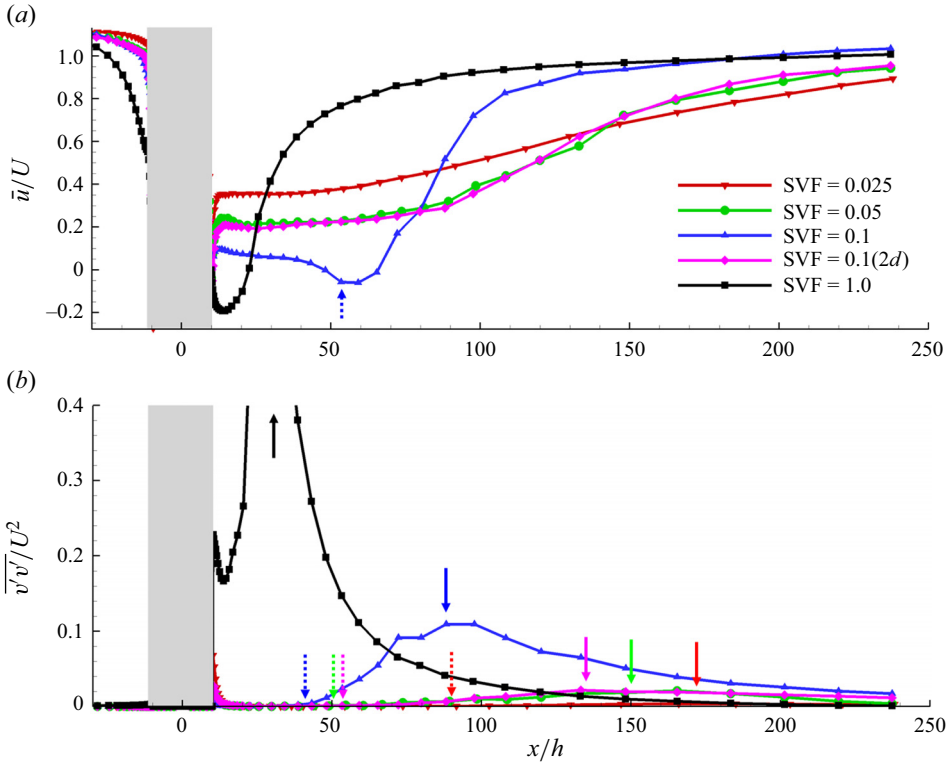
Figure 11. Longitudinal profiles of: (*a*) mean streamwise velocity, $\bar{u}/U$; and (*b*) spanwise normal stress, $\overline{v'v'}/U^2$, at the top boundary. The profiles are shown along the centreline, $y/D = 0$. The grey region shows the extent of the array region ($-10 < x/D < 10$). The dashed arrows in panels (*a*) and (*b*) show the end of the steady wake region based on the predicted values of L_{sw}/h and L'_{sw}/h, respectively. The solid arrows in panel (*b*) show the end of the total wake region based on the predicted values of L'_w/h.
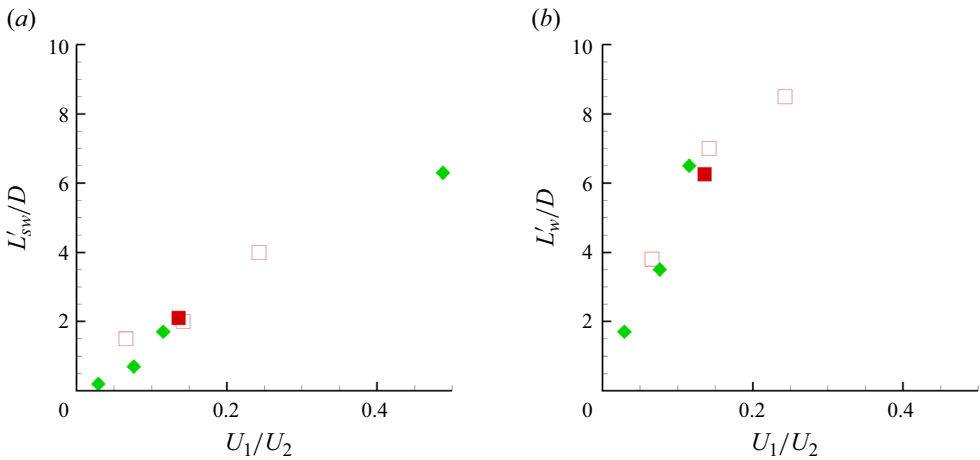

Figure 12. Variation of the length of the near-wake region with the velocity ratio U_1/U_2. (*a*) Steady wake length, L'_{sw}/D; (*b*) total wake length, L'_w/D. In addition to the present test cases ($D/h = 20$) with $d = 0.0125D$ (open red squares) and $d = 0.025D$ (solid red squares), results are also included for DES conducted for an array with $D/h = 2.5$–3.3 (solid green diamonds) by Chang *et al.* (2017).
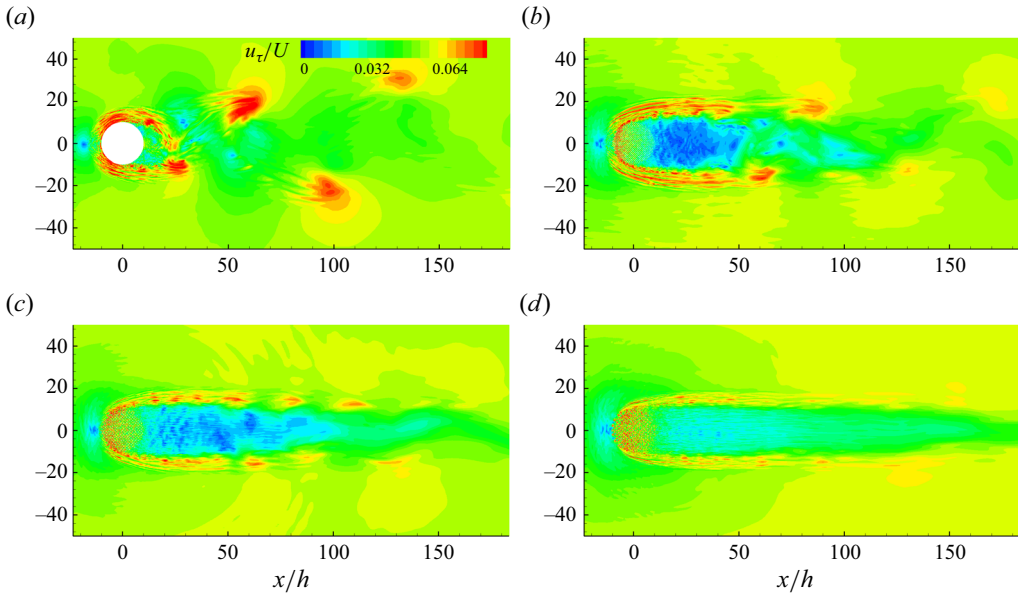
Figure 13. Non-dimensional bed friction velocity magnitude, u_τ/U, in the instantaneous flow. (*a*) SVF = 1.0; (*b*) SVF = 0.1; (*c*) SVF = 0.05; (*d*) SVF = 0.025.

instantaneous bed friction velocity with respect to the time-averaged value. The effect of these fluctuations on the capacity of the flow to entrain sediment can be quantified in an approximative way by the standard deviation of the bed friction velocity, u_τ^{SD} (Sumer *et al.* 2003). This is also why many RANS codes used to perform simulations with a deformable loose bed employ an 'enhanced' value of the bed shear stress, or equivalently of the bed friction velocity ($u_{\tau e} = \bar{u}_\tau + C'u_\tau^{SD}$), in the equation used to estimate the local flux of entrained sediment, where the value of the constant C' is of the order of one (Cheng, Koken & Constantinescu 2018). Following Chang *et al.* (2017), the magnitude of the local bed friction velocity in the instantaneous flow is calculated as $u_\tau/U = ((1/Re)((u_m/U)/(n_1/h)))^{1/2}$, where u_m is the instantaneous velocity magnitude in a plane parallel to the bed situated at a normal distance n_1 from the bed. The distance n_1 is sufficiently small for the plane to cut through the viscous sub-layer. The same definition is used to calculate $\bar{u}_\tau$ and u_τ^{SD} with u_m being the mean velocity magnitude and the square root of the turbulent kinetic energy, respectively.

Similar to the case of solid circular cylinders placed on a surface with $D/h \le O(1)$, most of the entrainment in the SVF = 1.0 case occurs beneath the regions of strong flow acceleration on the sides of the cylinder and beneath the cores of the wake roller vortices (see bed friction velocity distributions in figures 13*a* and 14*a*). When non-dimensionalized with the diameter of the cylinder, the width of the region of high u_τ/U forming on the side of the cylinder and the mean diameter of the regions of high u_τ/U forming beneath the cores of the wake rollers are approximately 30 % smaller in the simulation conducted with $D/h = 20$ compared with the values in the corresponding $D/h = 2.5$ solid cylinder simulation discussed by Chang *et al.* (2017). The peak bed friction velocity values inside these regions are also smaller in the $D/h = 20$ simulation. This means that the flux of entrained sediment from the bed around the solid cylinder decreases with increasing flow shallowness when normalized by the area of the cylinder.
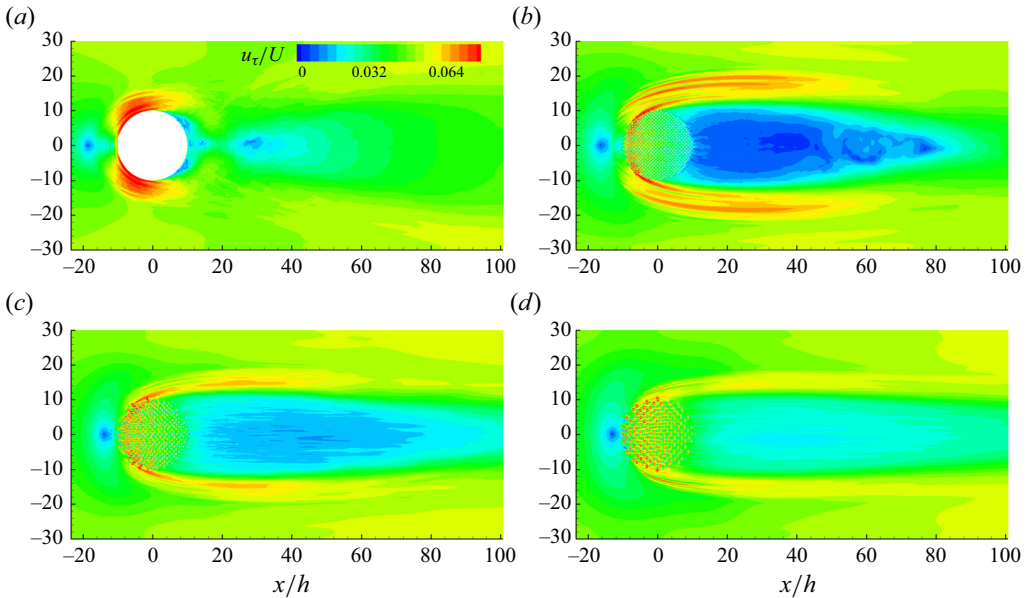
Figure 14. Non-dimensional bed friction velocity magnitude, $\overline{u_\tau}/U$, in the mean flow. (*a*) SVF = 1.0; (*b*) SVF = 0.1; (*c*) SVF = 0.05; (*d*) SVF = 0.025.

Similar trends are observed in the variation of the bed friction velocity in the vicinity and in the wake of the array for cases with SVF < 1. The main difference between the simulations performed with $D/h = 20$ and those with $2.5 \leq D/h \leq 3.3$ is the relatively larger amplification of the mean and instantaneous bed friction velocity on the outer side of the separated shear layers (e.g. see figures 13*b* and 14*b* for SVF = 0.1) where strongly coherent horseshoe vortices are present in some of the simulations (figure 2). In general, the cores of the HVs have a larger capacity to locally amplify the bed shear stress with increasing flow shallowness. Their increased size relative to the flow depth in the $D/h = 20$ simulations allows them to advect high streamwise velocity fluid from the immediate vicinity of the top boundary towards the bed. This is the main mechanics for the amplification of u_τ in this region (e.g. see figure 13*b*). Another difference with the simulations of Chang *et al.* (2017) conducted with $2.5 \leq D/h \leq 3.3$ is that the wake rollers and their trajectories are more regular in the $D/h = 20$ simulations. This also explains the fairly regular staggered pattern of the regions of high u_τ/U inside the near wake in figure 13(*a–c*). For cases where the antisymmetric wake shedding mode is very weak (SVF = 0.05 case) or absent (SVF = 0.025 case), most of the sediment entrained in the wake of the array originates in the thin elongated regions starting beneath the separated shear layers (figures 13*c,d* and 14*c,d*). The passage of the wake rollers and the movement of the HVs are the main mechanisms for the amplification the bed friction velocities outside of the array. Overall, the $D/h = 20$ simulations are characterized by rather regular trajectories of the larger-scale eddies originating inside the separated shear layers.

The regions of high u_τ^{SD}/U in figure 15 correlate well with the regions of high TKE in figure 9. As the SVF and aD decrease, u_τ^{SD}/U decreases around the upstream face of the array and inside its wake (figure 15), which is consistent with the observed decrease in the coherence of the HVs, the increase in the length of the separated shear layers and the decrease in the strength of the antisymmetric wake shedding mode. The positions and sizes of the regions of high u_τ^{SD}/U inside the array also vary with decreasing SVF and aD.
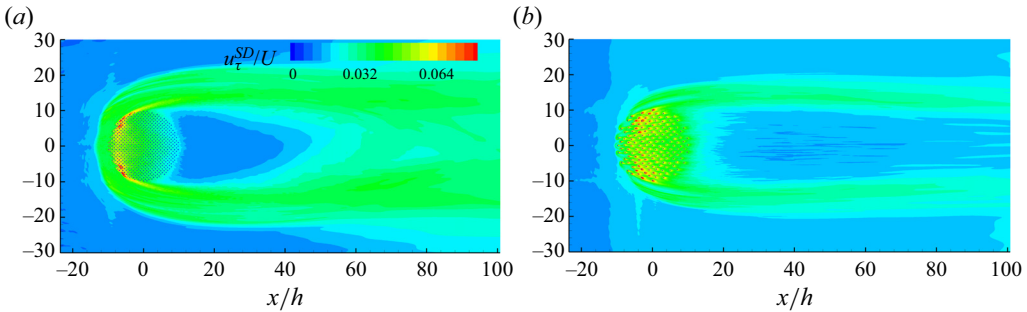
995 A9-22

Figure 15. Non-dimensional root mean square of the bed friction velocity magnitude, u_τ^{SD}/U. (*a*) SVF = 1.0; (*b*) SVF = 0.025.

These changes are driven by the positions and number of cylinders that generate strong wake vortex shedding. A decrease of the SVF increases the percentage of the cylinders in the array that generate strong vortex shedding.

One way to assess in a more quantitative way the effect of varying aD and SVF on the sediment entrainment capacity of the flow inside the array and over the whole region affected by the presence of the cylinders inside the channel is to calculate the time-averaged flux of entrained sediment, $\overline{E_\tau}$. This variable is defined as the time-averaged value of the flux evaluated from the instantaneous flow fields, $E_\tau(t)$. Sediment entrainment formulae for non-cohesive sediment generally assume that E_τ is proportional to $(u_\tau^2 - u_{\tau cr}^2)^\gamma$ with $\gamma > 1$, where $u_{\tau cr}$ is the critical value for sediment entrainment for a given mean particle diameter, d_{50}. The value of γ is 1.5 in van Rijn's (1984) formula which is often used to estimate the volumetric flux in eddy-resolving simulations with a movable bed (e.g. see Chou & Fringer 2010). In non-dimensional form, the volumetric flux of sediment entrained from the bed can be written as

$$E_\tau(tU/D) = \frac{1}{D^2} \int_{A'} \frac{(u_\tau^2 - u_{\tau cr}^2)^{1.5} \, \mathrm{d}A}{U^3}, \tag{5.1}$$

where A is the area over which entrainment is calculated and $A'(t)$ is the region of the bed where $u_\tau(t, x, y) > u_{\tau cr}$. Figure 16 includes three values of $\overline{E_\tau}$ calculated assuming the area A is the whole channel bed, the bed region situated inside the array and the bed region situated outside the array. Results are reported for $u_{\tau cr}/U = 0.065$ (critical bed shear stress $\tau_{cr}/\rho U^2 = 0.0042$) such that no sediment is entrained at large distances from the array. The values of $\overline{E_\tau}$ inside and outside the array are not close in the two simulations conducted with $aD \approx 1$. This means that the entrainment flux is a function of both SVF and the relative size of the cylinders forming the array. For constant aD, the fluxes entrained inside and outside the array are larger in the simulation conducted with cylinders of larger diameter (e.g. in the SVF = 0.1(2*d*) case compared with the SVF = 0.05 case). For constant SVF, the flux of sediment entrained outside the array decreases with increasing diameter of the solid cylinder, while the opposite trend is observed for the flux of sediment entrained inside the array. For constant d/D, the flux of sediment entrained outside the array increases monotonically with the SVF and aD. The main reasons are the increased size of the region of strong flow acceleration forming on the sides of the array for $|\phi| > 30°$ and the increased near-bed velocity magnitudes inside this region. However, the velocity of the flow entering the array increases with decreasing SVF and aD. The opposite is true for the streamwise rate of decrease of the velocity in between the cylinders. These varying trends explain the
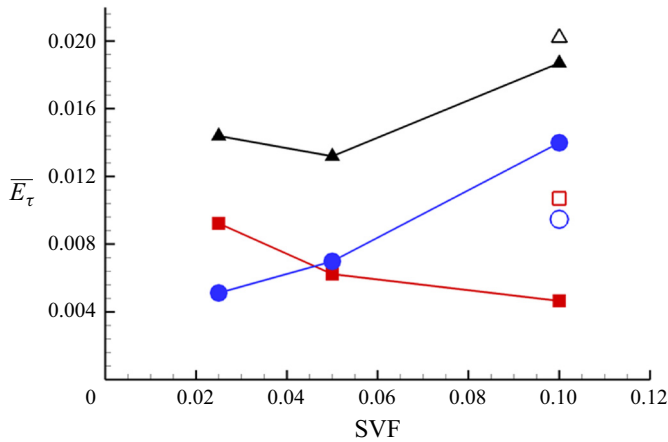
Figure 16. Non-dimensional flux of entrained sediment, $\overline{E_\tau}$, as a function of the solid volume fraction, SVF. The red line and red solid symbols show $\overline{E_\tau}$ calculated inside the array. The blue line and blue solid symbols show $\overline{E_\tau}$ calculated outside the array. The black line and black solid symbols show $\overline{E_\tau}$ calculated over the whole channel bed. The open symbols correspond to the SVF $= 0.1(2d)$ case. Results are plotted for a critical bed friction velocity, $u_{\tau c}/U = 0.065$.

monotonic decay of $\overline{E_\tau}$ with increasing SVF in figure 16 for the simulations conducted with constant d. Given the opposite variations of $\overline{E_\tau}$ inside and outside the array, the total sediment flux entrained over the whole bed reaches a minimum around SVF $= 0.05$. This value of the SVF roughly corresponds to the transition between a regime where counter-rotating roller vortices form and a regime where such vortices do not form.

6. Drag forces

For moderately shallow conditions and a sufficiently large value of aD such that the antisymmetric vortex shedding mode is strong, Chang *et al.* (2017) found that most of the total drag is due to drag forces acting on the cylinders directly exposed to the incoming flow and those situated in their immediate vicinity. Present results show this is also the case for very shallow flow conditions if $aD \geq 10$. As aD decreases to values where the antisymmetric shedding mode is very weak or absent, all cylinders are subject to significant drag forces.

Figure 17 shows a plot of the mean streamwise drag force on the solid cylinders normalized by the drag force acting on an isolated cylinder. This information is especially valuable in the case of patches of aquatic vegetation where the movement of the plant stems, and the capacity of the plant stems to avoid dislocation from the bed are a function of the magnitude of the drag force acting on them. The distribution of the normalized streamwise drag force is qualitatively different in the SVF $= 0.1$ case ($aD = 10.2$) with respect to the other cases. In the SVF $= 0.1$ case, more than 60 % of the cylinders in the array are subject to fairly negligible drag forces defined as forces that are less than 20 % of the force acting on an isolated cylinder of same diameter for the same value of Re_d. Interestingly, most of the cylinders directly exposed to the incoming flow are also subject to streamwise drag forces smaller by approximately 20–40 % compared with the force acting on an isolated cylinder. This is because the cylinders situated close to the frontal face of the array contribute to the deceleration of the flow as it approaches the array and this deceleration is stronger than that for an isolated cylinder, especially for relatively large
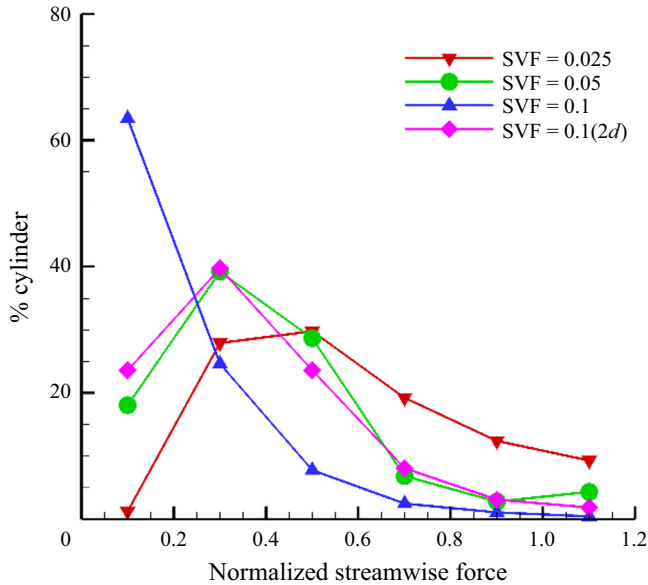
Figure 17. Distribution of the normalized mean streamwise drag force acting on the solid cylinders forming the array. The force on each cylinder is normalized by the drag force acting on an isolated solid cylinder. The vertical axis shows the percentage of the cylinders forming the array for which the normalized drag force is in between $(2i)/10$ and $(2i + 2)/10$ with $i = 0$ to 5.

values of aD. As aD decreases, the percentage of the cylinders for which the drag force is less than 20 % of the force acting on an isolated one decreases to 20 % for $aD \approx 5$ and to 0 % for $aD \approx 2.5$. For $aD < 5$, 30 % to 40 % of the cylinders are subject to drag forces that are approximately 30 % to 50 % of the drag force acting on an isolated cylinder, with a very small number of cylinders (less than 5 %) being subject to drag forces that are comparable or larger than that acting on an isolated cylinder. It is only for sufficiently small values of aD, when no rollers form in the wake, that the number of cylinders subject to forces that are comparable to, or larger than, the one acting on an isolated cylinder becomes important. This percentage is close to 20 % for $aD = 0.05$. Though drag forces on the individual cylinders in the SVF $= 0.1(2d)$ case are much larger than those in the SVF $= 0.05$ case, the distributions of the normalized drag forces are close to identical in the two cases. This shows that the distribution of the normalized drag forces inside the array is mainly a function of aD.

The time-averaged, total streamwise drag force acting on the array is also mainly a function of aD. The variation of this force with aD is plotted in non-dimensional form in figure 18(*a*). A total drag coefficient for the array is defined, $\bar{C}_{DG} = \bar{F}_x/(0.5\rho U^2 Dh)$, where $\bar{F}_x$ is the total streamwise drag force acting on the N cylinders forming the array. For the range of aD values considered in the present study, $\bar{C}_{DG}$ increases monotonically with aD, though the rate of increase gradually reduces for the larger values of aD. In addition to the total streamwise drag force acting on the array, a common measure of the drag acting on the array is the average non-dimensional streamwise drag force acting on the solid cylinders, $\bar{C}_d = (\bar{C}_{DG}/N)(D/d) = (1/N)\sum_{n=1}^{N} \bar{C}_D^n$, where $\bar{C}_D^n = \bar{F}_x^n/(0.5\rho U^2 dh)$ is the non-dimensional streamwise drag force acting on the rank n cylinder in the array ($n = 1$ to N). Though the instantaneous values of the streamwise drag force acting on the cylinders directly exposed to the incoming flow and to those in their vicinity can be
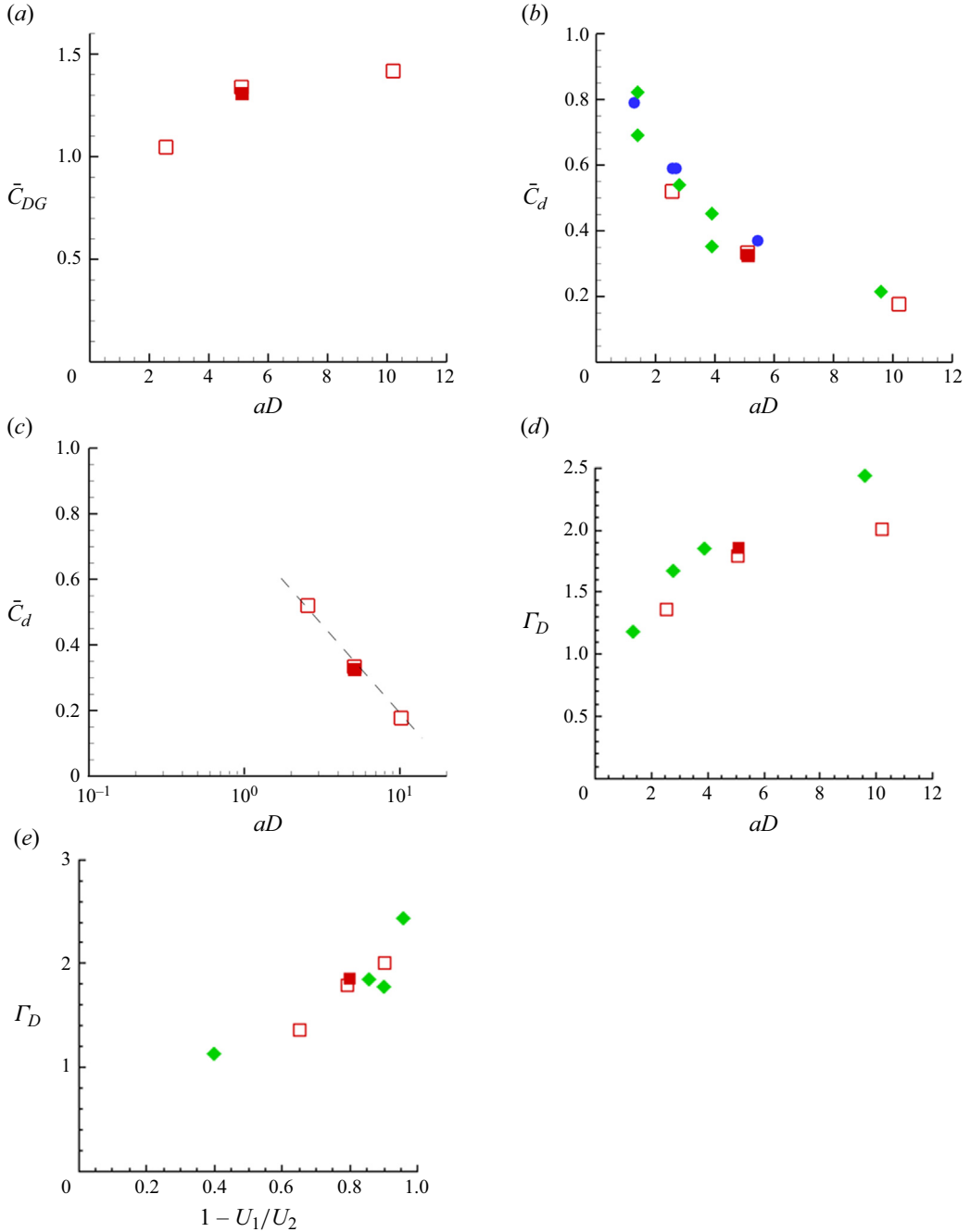
Figure 18. Non-dimensional time-averaged streamwise drag force. (*a*) Time-averaged total drag coefficient for the array, $\bar{C}_{DG}$ versus aD; (*b*) mean, time-averaged solid cylinder drag coefficient, $\bar{C}_d = (\bar{C}_{DG}/N)(D/d)$ versus aD; (*c*) $\bar{C}_d$ versus aD in log-linear scale; (*d*) combined drag parameter for the array, $\Gamma_D = \bar{C}_d(aD)/(1 - \text{SVF})$ versus aD; (*e*) Γ_D versus $1 - U_1/U_2$. In addition to the present test cases ($D/h = 20$) with $d = 0.0125D$ (open squares) and $d = 0.025D$ (solid squares), some of the frames show data from the 3-D LES predictions of Chang & Constantinescu (2015) conducted for an array of long porous cylinders (solid blue circles) and the 3-D DES of Chang *et al.* (2017) conducted for arrays with $D/h = 2.5$ and 3.3 (solid green diamonds). The dashed line in panel (*c*) shows a best fit to the numerical data, $\bar{C}_d = 0.75 - 0.248 * \ln(aD)$.

a couple of times larger than the mean value, the peak values of the instantaneous total streamwise drag force, or equivalently of the total drag coefficient, C_{DG}, are of the order of 10 % of the corresponding time-averaged value (e.g. $\bar{C}_{DG}$). The largest fluctuations of the total non-dimensional streamwise drag force acting on the array are predicted in the SVF = 0.025 case and in the SVF = 0.1(2d) case. For these two cases, the maximum values of the instantaneous total spanwise force acting on the array are approximately 10 % of the time-averaged value of the total streamwise drag force.

As shown in figure 18(b,c), $\bar{C}_d$ decreases with aD and the decrease is close to logarithmic. Figure 18(b) also includes the predictions of $\bar{C}_d$ from the numerical simulations of Chang *et al.* (2017) and Chang & Constantinescu (2015) performed for arrays with $aD < 5$ and for arrays of long cylinders, respectively. Overall, the values for the present simulation performed for $D/h = 20$ are slightly lower than those in the other two numerical studies. So, increasing flow shallowness slightly reduces the mean non-dimensional drag force acting on the cylinders forming the array. This effect is even stronger for the combined drag parameter for the array, $\Gamma_D = \bar{C}_d aD/(1 - \text{SVF})$, shown in figure 18($d$). This variable characterizes the relative influence of the drag term relative to the advection term (Chang & Constantinescu 2015). It also represents the ratio of the array diameter, D, to the array's drag length scale, $L_c = 2(1 - \text{SVF})/(\bar{C}_d \cdot a)$. Increasing D/h from 3 to 20 results in a decrease of up to 25 % of Γ_D for $aD \approx 10$. The decrease is less than 7 % for $aD < 3$. So, for this variable flow, shallowness effects are also a function of aD. The combined drag parameter characterizes the overall flow deceleration inside the array, which is of the order of the difference between the incoming velocity, U_0 and the bleeding velocity at the back of the array, U_1. Results in figure 18(e) confirm that Γ_D increases close to monotonically with $1 - U_1/U_0$ and that a unique curve can be used to describe this variation for both moderately shallow and very shallow flow conditions.

7. Summary and conclusions

The present study showed that several important qualitative and quantitative changes occur in the flow and turbulence structure generated by a circular array of emerged cylinders in an open channel in between cases with moderately shallow flow conditions ($1 < D/h < 5$) and cases with very shallow flow conditions ($D/h > 10$). The paper focused on cases where the stability number was low enough such that roller vortices can still form in the wake for $D/h = 20$. This is the case of most significance for practical applications related to flow in shallow rivers containing vegetated patches away from their boundaries.

The main two qualitative changes associated with the increase in flow shallowness were the formation of a turbulent horseshoe vortex system containing multiple, strongly coherent vortices (up to 5) and the formation of arrays of parallel, co-rotating horizontal vortices in the vicinity of the roller vortices for sufficiently large values of aD. The dynamics of the horseshoe vortices was fairly similar to that of the laminar breakaway sub-regime observed for solid cylinders The present simulations showed that for sufficiently low aD (e.g. $aD < 10$), the horseshoe vortices lose their coherence for small polar angles, with the peak coherence occurring for polar angle magnitudes between 40° and 90°. This result is not as surprising given that main necklace vortices of low coherence near the symmetry plane were also observed for flow over a high-aspect-ratio rectangular cylinder. In the latter case, the coherence of the turbulent horseshoe vortices was the highest around the lateral edges of the cylinder rather than close to its symmetry plane (Kirkil & Constantinescu 2009). Only for relatively large values of aD, the main necklace vortex remained strongly coherent over all the frontal side of the array with $D/h = 20$. By contrast, for cases with $D/h < 5$, the turbulent horseshoe vortex system was

found to contain only one main vortex whose coherence is the largest in the symmetry ($\phi = 0°$) plane. The other main difference with arrays with $D/h < 5$ was that the cores of the main horseshoe vortices extended over most of the flow depth. So, their interactions with the eddies shed in the separated shear layers occurred over the whole flow depth rather than being confined to the near-bed region. The present study showed that this is a main condition for the eventual formation of a secondary, near-wake instability in the form of array of horizontal, parallel vortices in the wake of a surface-mounted porous obstruction.

For comparable values of aD, increasing the flow shallowness resulted in a decrease of the strength of the upwelling and downwelling motions inside the array. This was accompanied by a decrease of the combined drag coefficient for the array, Γ_D, and thus of the overall flow deceleration inside the array, with the effects being stronger for relatively large values of aD. Meanwhile, the variation of the mean, time-averaged streamwise drag coefficient of the solid cylinders, $\bar{C}_d$, with aD was only mildly affected by varying D/h. Increasing the flow shallowness also triggered an increase in the width (e.g. up to $7.5h$ or $0.375D$ in the SVF $= 0.1$ case) of the region where the erosive capacity of the horseshoe vortices is large. The near wake was also affected by flow shallowness. Most notably, an increase in the length of the separation bubble and of the degree of vertical non-uniformity of the mean flow were observed for relatively large values of aD. Meanwhile, the minimum value of aD (≈ 6.0) required for a bubble to form behind the array was found to be independent of D/h. The increase in the length of the separation bubble with D/h was accompanied by an increase of the non-dimensional length of the total wake, L'_w/D. A strong increase of the Strouhal number associated with the formation and passage of roller vortices with D/h was observed for relatively low values of aD (e.g. $St \approx 0.4$ for $aD \approx 5$). This result is quite interesting given that the Strouhal number for solid cylinders was found to be largely unaffected by the increase in D/h (Zeng & Constantinescu 2017).

Declaration of interest. The authors report no conflict of interest.

Author ORCID.

Ⓓ George Constantinescu https://orcid.org/0000-0001-7060-8378.

REFERENCES

AKILLI, H. & ROCKWELL, D. 2002 Vortex formation from a cylinder in shallow water. *Phys. Fluids* **14** (9), 2957–2967.

BALACHANDAR, R., CHU, V.H. & ZHANG, J. 1997 Experimental study of turbulent concentration flow field in the wake of a bluff body. *J. Fluids Engng* **199**, 263–272.

BALACHANDAR, R., RAMACHANDRAN, S. & TACHIE, M. 2000 Characteristics of shallow turbulent near wakes at low Reynolds numbers. *J. Fluids Engng* **122**, 302–311.

BOUMA, T.J., VAN DUREN, L.A., TEMMERMAN, S., CLAVERIE, T., BLANCO-GARCIA, A., YSEBAERT, T. & HERMAN, P. 2007 Spatial flow and sedimentation patterns within patches of epibenthic structures: combining field, flume and modelling experiment. *Cont. Shelf Res.* **27** (8), 1020–1045.

CAMPOREALE, C., PERUCCA, E., RIDOLFI, L. & GURNELL, A.M. 2013 Modelling the interactions between river morphodynamics and riparian vegetation. *Rev. Geophys.* **51**, 379–414.

CARMER, C., RUMMEL, A.C. & JIRKA, G.H. 2009 Mass transport in shallow turbulent wake flow by planar concentration analysis technique. *J. Hydraul. Engng* **135** (4), 257–270.

CARR, G.M., DUTHIE, H.C. & TAYLOR, W.D. 1997 Models of aquatic plant productivity: a review of the factors that influence growth. *Aquat. Bot.* **59**, 195–215.

CHANG, K., CONSTANTINESCU, G. & PARK, S.O. 2007 Assessment of predictive capabilities of Detached Eddy Simulation to simulate flow and mass transport past open cavities. *ASME J. Fluids Engng* **129** (11), 1372–1383.

CHANG, K.S. & CONSTANTINESCU, G. 2015 Numerical investigation of flow and turbulence structure through and around a circular array of rigid cylinders. *J. Fluid Mech.* **776**, 161–199.

CHANG, W.Y., CONSTANTINESCU, G. & TSAI, W.Y. 2017 On the flow and coherent structures generated by an array of rigid energed cylinders place in an open channel with flat and deformed bed. *J. Fluid Mech.* **831**, 1–40.

CHANG, W.Y., CONSTANTINESCU, G. & TSAI, W.F. 2020 Effect of array submergence on flow and coherent structures through and around a circular array of rigid vertical cylinders. *Phys. Fluids* **32**, 035110.

CHEN, D. & JIRKA, G.H. 1995 Experimental study of plane turbulent wakes in a shallow water layer. *Fluid Dyn. Res.* **16**, 11–41.

CHEN, Z., ORTIZ, A., ZONG, L. & NEPF, H. 2012 The wake structure behind a porous obstruction and its implications for deposition near a finite patch of emergent vegetation. *Water Resour. Res.* **48**, W09517.

CHENG, Z. & CONSTANTINESCU, G. 2020 Near-field and far-field structure of shallow mixing layers. *J. Fluid Mech.* **904**, A21.

CHENG, Z., KOKEN, M. & CONSTANTINESCU, G. 2018 Approximate methodology to account for effects of coherent structures on sediment entrainment in RANS simulations with a movable bed and applications to pier scour. *Adv. Water Resour.* **120**, 65–82.

CHOU, Y. & FRINGER, O. 2010 A model for the simulation of coupled flow-bed form evolution in turbulent flows. *J. Geophys. Res.* **115**, 0148–0227.

CONSTANTINESCU, G. 2014 LE of shallow mixing interfaces: a review. *Environ. Fluid Mech.* **14** (5), 971–996.

CORENBLIT, D., TABACCHI, E., STEIGER, J. & GURNELL, A.M. 2007 Reciprocal interactions and adjustments between fluvial landforms and vegetation dynamics in river corridors: a review of complementary approaches. *Earth Sci. Rev.* **84**, 56–86.

COSTANZA, R., *et al.* 1997 The value of the world's ecosystem services and natural capital. *Nature* **387** (6630), 253–260.

FOLLETT, E. & NEPF, H. 2012 Sediment patterns near a model patch of reedy emergent vegetation. *Geomorphology* **179**, 141–151.

GRUBISIC, V., SMITH, R.B. & SCHAR, C. 1995 The effect of bottom friction on shallow-flow past an isolated obstacle. *J. Atmos. Sci.* **48**, 1985–1998.

GURNELL, A., TOCKNER, K., EDWARDS, A. & PETTS, G. 2005 Effects of deposited wood on biocomplexity of river corridors. *Front. Ecol. Environ.* **3** (7), 377–382.

GURNELL, A.M. 2014 Plants as river system engineers. *Earth Surf. Process. Landf.* **39** (1), 4–25.

HAMED, A.M., SADOWSKI, M.J., NEPF, H.M. & CHAMORRO, L.P. 2017 Impact of height heterogeneity on canopy turbulence. *J. Fluid Mech.* **813**, 1176–1196.

HONG, L., CHENG, S., HOUSEAGO, R.C., PARSONS, D.R. & CHAMORRO, L.P. 2022 On the submerged low-Cauchy-number canopy dynamics under unidirectional flows. *J. Fluids Struct.* **113**, 103646.

HORPPILA, J. & NURMINEN, L. 2003 Effects of submerged macrophytes on sediment resuspension and internal phosphorus loading in Lake Hiidenvesi (southern Finland). *Water Res. Res.* **37**, 4468–4474.

HOUSEAGO, R.C., HONG, L., CHENG, S., BEST, J.L., PARSONS, D.R. & CHAMORRO, L.P. 2022 On the turbulence dynamics induced by a surrogate seagrass canopy. *J Fluid Mech.* **934**, A17.

HUAI, W., XUE, W. & QIAN, Z. 2015 Large-eddy simulation of turbulent rectangular open-channel flow with an emerged rigid vegetation patch. *Adv. Water Resour.* **80**, 30–42.

INGRAM, G.R. & CHU, V.H. 1987 Flow around islands in Rupert bay: an investigation of the bottom friction effect. *J. Geophys. Res. Atmos.* **92**, 14521.

JONES, C., LAWTON, J. & SCHACHAK, M. 1994 Organisms as ecosystem engineers. *Oikos* **69**, 373–386.

KIM, H.S., KIMURA, I. & SHIMIZU, Y. 2015 Bed morphological changes around a finite patch of vegetation. *Earth Surf. Process. Landf.* **40** (3), 375–388.

KIRKIL, G. & CONSTANTINESCU, G. 2009 Nature of flow and turbulence structure around an in-stream vertical plate in a shallow channel and the implications for sediment erosion. *Water Resour. Res.* **45**, W06412.

KIRKIL, G. & CONSTANTINESCU, G. 2012 The laminar necklace vortex system and wake structure in a shallow channel flow past a bottom-mounted circular cylinder. *Phys. Fluids* **24**, 073602.

KIRKIL, G. & CONSTANTINESCU, G. 2015 Effects of cylinder Reynolds number on the turbulent horseshoe vortex system and near wake of a surface-mounted circular cylinder. *Phys. Fluids* **27**, 075102.

KOKEN, M. & CONSTANTINESCU, G. 2020 Flow structure inside and around a rectangular array of rigid, emerged cylinders located at the sidewall of an open channel. *J. Fluid Mech.* **910**, A2.

KOKEN, M. & CONSTANTINESCU, G. 2023 Influence of submergence ratio on flow and drag forces generated by a long rectangular array of rigid cylinders at the sidewall of an open channel. *J. Fluid Mech.* **966**, A5.

LEI, J. & NEPF, H. 2021 Evolution of velocity from leading edge of 2D and 3D submerged canopies. *J. Fluid Mech.* **916**, A36.

LIU, C., HU, Z., LEI, J. & NEPF, H. 2017 Vortex structure and sediment deposition in the wake behind a finite patch of submerged vegetation. *J. Hydraul. Engng* **144** (2), 04017065.

LIU, C. & NEPF, H.M. 2016 Sediment deposition within and around a finite patch of model vegetation over a range of channel velocity. *Water Resour. Res.* **52** (1), 600–612.

LIU, D., DIPLAS, P., FAIRBANKS, J.D. & HODGES, C.C. 2008 An experimental study of flow through rigid vegetation. *J. Geophys. Res. Earth Sci.* **113**, 1–16.

LIU, M.Y., HUAI, W.X., JI, B. & HAN, P. 2021 Numerical study on the drag characteristics of rigid submerged vegetation patches. *Phys. Fluids* **33** (8), 085123.

MONTI, A., OMIDYEGANEH, M., ECKHARDT, B. & PINELLI, A. 2020 On the genesis of different regimes in canopy flows: a numerical investigation. *J. Fluid Mech.* **891**, A9.

MONTI, A., OMIDYEGANEH, M. & PINELLI, A. 2019 Large-eddy simulation of an open-channel flow bounded by a semi-dense rigid filamentous canopy: scaling and flow structure. *Phys. Fluids* **31**, 065108.

NEGRETTI, M.E., SOCOLOFSKY, S., RUMMEL, A. & JIRKA, G.H. 2005 Stabilization of cylinder wakes in shallow water flows by means of roughness elements: an experimental study. *Exp. Fluids* **38**, 403–414.

NEPF, H.M. 2012 Flow and transport in regions with aquatic vegetation. *Annu. Rev. Fluid Mech.* **44**, 123–142.

PAN, Y., FOLLETT, E., CHAMECKI, M. & NEPF, H. 2014 Strong and weak, unsteady reconfiguration and its impact on turbulence structure within plant canopies. *Phys. Fluids* **26**, 105102.

PLEW, D.R., COOPER, G.C. & CALLAGHAN, F.M. 2008 Turbulence-induced forces in a freshwater macrophyte canopy. *Water Resour. Res.* **44**, W02414.

PRINZ, F., BREVIS, W. & SOCOLOFSKY, S. 2012 Shallow wake formed after porous structures: quantification of the influence of porosity on the flow characteristics. *CD-ROM Proceedings of the 3rd International Symposium of Shallow Flows, IA, USA*.

RIGHETTI, M. & ARMANINI, A. 2002 Flow resistance in open channel flows with sparsely distributed bushes. *J. Hydrol.* **269**, 55–64.

VAN RIJN, L.C. 1984 Sediment pick-up functions. *Journal of Hydraulic Engineering* **110** (10), 1494–1502.

RODI, W., CONSTANTINESCU, G. & STOESSER, T. 2013 *Large Eddy Simulation in Hydraulics*. IAHR Monograph. CRC Press.

ROMINGER, J.T., LIGHTBODY, A.F. & NEPF, H. 2010 Effects of added vegetation on sand bar stability and stream hydrodynamics. *J. Hydraul. Engng* **136** (12), 994–1002.

ROMINGER, J.T. & NEPF, H. 2011 Flow adjustment and interior flow associated with a rectangular obstruction. *J. Fluid Mech.* **680**, 636–659.

ROCKWELL, D. 2008 Vortex formation in shallow flows. *Phys. Fluids* **20**, 031303.

SAND-JENSEN, K. & PEDERSEN, M.L. 2008 Streamlining of plant patches in streams. *Freshwater Biol.* **53**, 714–726.

SCHOELYNCK, J., DE GROOTE, T., BAL, K., VANDENBRUWAENE, W., MEIRE, P. & TEMMERMAN, S. 2012 Self-organized patchiness and scale-dependent bio-geomorphic feedbacks in aquatic river vegetation. *Ecography* **35**, 760–768.

SCHULTZ, M., KOZERSKI, H.-P., PLUNTKE, T. & RINKE, K. 2003 The influence of macrophytes on sedimentation and nutrient retention in the lower river spree. *Water Resour. Res.* **37**, 569–578.

SOCOLOFSKY, S.A., CARMER, C. & JIRKA, G.H. 2004 Shallow turbulent wakes: linear stability analysis compared to experimental data. In *Shallow Flows* (ed. G.H. Jirka & W.S.J Uijttewaal), pp. 31–38. A.A. Balkema.

SOCOLOFSKY, S.A. & JIRKA, G.H. 2004 Large scale flow structures and stability in shallow flows. *J. Environ. Engng Sci.* **3**, 451–462.

SOULIOTIS, D. & PRINOS, P. 2010 Macroscopic turbulence models and their application in turbulent vegetated flows. *J. Hydraul. Engng* **137** (3), 314–332.

SPALART, P. 2009 Detached eddy simulation. *Annu. Rev. Fluid Mech.* **41**, 181–202.

SPALART, P. & ALLMARAS, S.R. 1992 A one equation turbulence model for aerodynamic flows. *AIAA Paper* 92-0439.

SUKHODOLOV, A. & SUKHODOLOVA, T. 2010 Case study: effect of submerged aquatic plants on turbulence structure in a lowland river. *J. Hydraul. Engng ASCE* **136** (7), 434–446.

SUKHODOLOV, A. & SUKHODOLOVA, T. 2014 Shallow wake behind exposed wood-induced bar in a gravel-bed river. *Environ. Fluid Mech.* **14** (5), 1071–1083.

SUMER, B., CHUA, L., CHENG, N. & FREDSØE, J. 2003 Influence of turbulence on bed load sediment transport. *J. Hydraul. Engng* **129** (8), 585–596.

TAL, M. & PAOLA, C. 2007. Dynamic single-thread channels maintained by the interaction of flow and vegetation. *Geol. Soc. Am.* **35**, 347–350.

VAN WESENBEECK, B.K., *et al.* 2008 Does scale-dependent feedback explain spatial complexity in salt-marsh ecosystems? *Oikos* **117**, 152–159.

WHITE, B.L. & NEPF, H. 2007 Shear instability and coherent structure in shallow flow adjacent to a porous layer. *J. Fluid Mech.* **593**, 1–32.

WILCOCK, R., CHAMPION, P., NAGELS, J. & CROCKER, G. 1999 The influence of aquatic macrophytes on the hydraulic and physico-chemical properties of a New Zealand lowland stream. *Hydrobiologia* **416**, 203–214.

YANG, J.Q., CHUNG, H. & NEPF, H. 2016 The onset of sediment transport in vegetated channels predicted by turbulent kinetic energy. *Geophys. Res. Lett.* **43** (11), 11261–11268.

ZENG, J. & CONSTANTINESCU, G. 2017 Flow and coherent structures around circular cylinders in shallow water. *Phys. Fluids* **29** (6), 066601.

ZENG, J., CONSTANTINESCU, G. & WEBER, L. 2008 A 3D non-hydrostatic model to predict flow and sediment transport in loose-bed channel bends. *J. Hydraul. Engng* **46** (3), 356–372.

ZONG, L. & NEPF, H. 2010 Flow and deposition in and around a finite patch of vegetation. *Geomorphology* **116** (3-4), 363–372.

ZONG, L. & NEPF, H. 2011 Spatial distribution of deposition within a patch of vegetation. *Water Resour. Res.* **47**, W03516.

ZONG, L. & NEPF, H. 2012 Vortex development behind a finite porous obstruction in a channel. *J. Fluid Mech.* **691**, 368–391.